

The Complex Organic Molecules of Embedded Protostars at Perseus

YAO-LUN YANG,^{1,2} NAMI SAKAI,² AND YICHEN ZHANG²

¹*Department of Astronomy, University of Virginia, Charlottesville, VA 22904-4235, USA*

²*RIKEN Cluster for Pioneering Research, Wako-shi, Saitama, 351-0106, Japan*

1. INTRODUCTION

Planet formation may start during the embedded phase of star formation. In the scenario where planets form from the embedded disks, resulting in substructures, the chemistry of embedded disks may play a significant role for the chemical composition of the forming planets. In the recent years, observations discover the emission of carbon-chain molecules and complex organic molecules (COMs) toward the center of several embedded protostars, indicating that embedded protostars have developed a complex chemistry at the disk-forming region. If the forming planets inherit the chemistry of embedded disks, the abundance of complex organic molecules may implicate future developments of organics on the planets.

Heavier or more complex molecules, such as cyclic-C₃H₂, SO, and complex organic molecules (COMs), are in the gas phase at the inner protostellar envelope ($T \gtrsim 100$ K), exclusively tracing the properties of the inner envelope where a disk may be forming (Aikawa 2013; Sakai et al. 2014). The kinematics of a rotating infalling envelope has been analyzed with the observations of heavier or more complex molecules, such as CH₃OH and CH₂DOH for HH 212 (Lee et al. 2017), CS for IRAS 04365+2535 (Sakai et al. 2016) and L483 (Oya et al. 2017), cyclic-C₃H₂ for L1527 (Sakai et al. 2014), OCS for IRAS 16293–2422 A (Oya et al. 2016), and methanol and HCOOH for B335 (Imai et al. 2019).

In the review by Herbst & van Dishoeck (2009), complex molecules are defined as carbon-bearing molecules that contain six atoms or more. Saturated complex molecules are rich in hydrogen atoms, often called complex organic molecules (COMs), while the unsaturated complex molecules are lack of hydrogen atoms, mostly in the form of long carbon-chain molecules. While recent observations show several embedded protostars with rich spectra of complex molecules, the occurrence of complex molecules at embedded protostars and its relation-

ship to the star formation process remain poorly understood. Several protostars are rich in COMs but show little emission of long carbon-chain molecules, such as IRAS 16293–2422 (Jørgensen et al. 2016), NGC 1333 IRAS 4A (Bottinelli et al. 2004), B335 (Imai et al. 2016, 2019), and BHR 71 (Yang et al. 2020 accepted); some protostars are rich in long carbon-chain molecules but not in COMs, such as L1527 (Sakai et al. 2010) and IRAS 15398–3359 (Sakai et al. 2009). While the bimodal chemical appearance hints a bimodal evolutionary path, the chemical evolution at the embedded protostars remain ill-constrained as a few protostars show the emission of both COMs and long carbon-chain molecules at different scales, such as L483 (Oya et al. 2017).

The Perseus ALMA Chemistry Survey (PEACHES) aims to provide the statistics on the occurrence of complex molecules at embedded protostars. This program unbiasedly observes 51 embedded protostars with ALMA around 260 GHz, covering the emission of simple molecules such as CS and H¹³CN as well as the emission of complex molecules including CH₃OH and CH₃OCHO.

2. OBSERVATIONS

Set3 has the continuum window ranging from 245800 MHz to 246730 MHz, while the Set1 and Set1 have the continuum window ranging from 246200 MHz to 247130 MHz.

3. SPECTRA EXTRACTION

The ALMA image cubes are post-processed to extract 1D spectra for identifying the emission of complex molecules and further analyses. COMs typically desorb from dust grains at $T \gtrsim 100$ K, which coincidentally corresponds to ~ 100 au for typical embedded protostars (e.g., Yang et al. 2020). Given the spatial resolution of $\sim 0''.5$ (~ 150 au), we focus on the spectra toward the continuum sources to search for the COMs in the inner envelope. Four steps of post-processing reduces the image cubes to 1D spectra, which are summarized below.

- Continuum fitting: We use the CASA task `imfit` to iteratively fit for continuum sources down to 5σ of the residual image within the central 70% of the

Table 1. PEACHES Sample

Source	Common names	R.A. (J2000)	Decl. (J2000)	v_{lsr}	Beam	Cont. Size	T_{cont}	Ref. (v_{lsr})
		(hh:mm:ss)	(dd:mm:ss)	(km s ⁻¹)	($''$)	($''$)	(K)	
Per-emb 22 B		03:25:22.35	30:45:13.11	4.3	0 $''$ 64 \times 0 $''$ 39	0 $''$ 95 \times 0 $''$ 51	0.92	S19
Per-emb 22 A		03:25:22.41	30:45:13.26	4.3	0 $''$ 64 \times 0 $''$ 39	0 $''$ 86 \times 0 $''$ 65	1.71	S19
L1448 NW	L1448 IRS 3C	03:25:35.67	30:45:34.16	4.2	0 $''$ 64 \times 0 $''$ 39	0 $''$ 83 \times 0 $''$ 47	3.15	H18
Per-emb 33 B/C		03:25:36.32	30:45:15.19	5.3	0 $''$ 64 \times 0 $''$ 39	0 $''$ 75 \times 0 $''$ 48	5.55	S19
Per-emb 33 A		03:25:36.38	30:45:14.72	5.3	0 $''$ 64 \times 0 $''$ 39	0 $''$ 73 \times 0 $''$ 45	10.33	S19
L1448 IRS 3A		03:25:36.50	30:45:21.90	4.6	0 $''$ 64 \times 0 $''$ 39	0 $''$ 85 \times 0 $''$ 59	3.21	H18
Per-emb 26		03:25:38.88	30:44:05.28	5.4	0 $''$ 64 \times 0 $''$ 39	0 $''$ 69 \times 0 $''$ 45	8.03	S19
Per-emb 42		03:25:39.14	30:43:57.90	5.8	0 $''$ 64 \times 0 $''$ 39	0 $''$ 64 \times 0 $''$ 39	0.66	S19
Per-emb 25	IRAS 03235+3004	03:26:37.51	30:15:27.81	5.5	0 $''$ 64 \times 0 $''$ 39	0 $''$ 69 \times 0 $''$ 41	5.27	S18
Per-emb 17	L1455 IRS 1, IRAS 03245+3002	03:27:39.11	30:13:02.96	6.0	0 $''$ 64 \times 0 $''$ 40	0 $''$ 79 \times 0 $''$ 48	2.00	S19
Per-emb 20	L1455 IRS 4	03:27:43.28	30:12:28.88	5.3	0 $''$ 64 \times 0 $''$ 40	1 $''$ 29 \times 0 $''$ 78	0.14	S19
L1455 IRS 2		03:27:47.69	30:12:04.33	5.1	0 $''$ 64 \times 0 $''$ 40	0 $''$ 60 \times 0 $''$ 38	0.13	H18
Per-emb 35 A	NGC 1333 IRAS 1	03:28:37.10	31:13:30.77	7.4	0 $''$ 66 \times 0 $''$ 42	0 $''$ 75 \times 0 $''$ 51	0.93	Y20
Per-emb 35 B	NGC 1333 IRAS 1	03:28:37.22	31:13:31.74	7.3	0 $''$ 66 \times 0 $''$ 42	0 $''$ 78 \times 0 $''$ 53	0.75	Y20
Per-emb 27	NGC 1333 IRAS 2A	03:28:55.57	31:14:36.97	6.5	0 $''$ 66 \times 0 $''$ 42	0 $''$ 93 \times 0 $''$ 66	5.79	Y20
EDJ2009-172		03:28:56.65	31:18:35.43	...	0 $''$ 66 \times 0 $''$ 42	0 $''$ 69 \times 0 $''$ 44	0.62	...
Per-emb 36	NGC 1333 IRAS 2B	03:28:57.37	31:14:15.77	6.9	0 $''$ 66 \times 0 $''$ 42	0 $''$ 73 \times 0 $''$ 46	5.56	S19
Per-emb 54	NGC 1333 IRAS 6	03:29:01.55	31:20:20.49	7.9	0 $''$ 66 \times 0 $''$ 42	0 $''$ 69 \times 0 $''$ 40	0.07	S19
SVS 13B	NGC 1333 SVS 13B	03:29:03.08	31:15:51.73	8.5	0 $''$ 66 \times 0 $''$ 42	0 $''$ 87 \times 0 $''$ 68	6.64	S19
SVS 13A2	VLA 3	03:29:03.39	31:16:01.58	8.4	0 $''$ 66 \times 0 $''$ 42	0 $''$ 86 \times 0 $''$ 53	0.61	S18
Per-emb 44	NGC 1333 SVS 13A	03:29:03.76	31:16:03.70	8.7	0 $''$ 66 \times 0 $''$ 42	0 $''$ 98 \times 0 $''$ 79	6.84	S19
Per-emb 15		03:29:04.06	31:14:46.23	6.8	0 $''$ 66 \times 0 $''$ 42	0 $''$ 89 \times 0 $''$ 70	0.17	S19
Per-emb 50	IRAS 03260+3111 A	03:29:07.77	31:21:57.11	9.3	0 $''$ 66 \times 0 $''$ 42	0 $''$ 73 \times 0 $''$ 44	4.13	Y20
Per-emb 12 B	NGC 1333 IRAS 4A2	03:29:10.44	31:13:32.08	6.9	0 $''$ 66 \times 0 $''$ 42	1 $''$ 33 \times 0 $''$ 81	10.04	S19
Per-emb 12 A	NGC 1333 IRAS 4A1	03:29:10.54	31:13:30.93	6.9	0 $''$ 66 \times 0 $''$ 42	1 $''$ 11 \times 0 $''$ 98	21.85	S19
Per-emb 21	NGC 1333 IRAS 7 SM2	03:29:10.67	31:18:20.16	8.6	0 $''$ 66 \times 0 $''$ 42	0 $''$ 74 \times 0 $''$ 48	2.05	Y20
Per-emb 18	NGC 1333 IRAS 7 SM1	03:29:11.27	31:18:31.09	8.1	0 $''$ 66 \times 0 $''$ 42	0 $''$ 84 \times 0 $''$ 73	3.42	S19
Per-emb 13	NGC 1333 IRAS 4B1	03:29:12.02	31:13:07.99	7.1	0 $''$ 66 \times 0 $''$ 42	1 $''$ 07 \times 0 $''$ 83	14.76	S19
IRAS4B'	NGC 1333 IRAS 4B2	03:29:12.85	31:13:06.87	7.1	0 $''$ 66 \times 0 $''$ 42	0 $''$ 83 \times 0 $''$ 74	7.13	S19
Per-emb 14	NGC 1333 IRAS 4C	03:29:13.55	31:13:58.12	7.9	0 $''$ 66 \times 0 $''$ 42	0 $''$ 79 \times 0 $''$ 50	3.05	S19
EDJ2009-235		03:29:18.26	31:23:19.73	7.7	0 $''$ 67 \times 0 $''$ 42	0 $''$ 66 \times 0 $''$ 44	0.26	Y20
EDJ2009-237		03:29:18.74	31:23:25.24	...	0 $''$ 67 \times 0 $''$ 42	0 $''$ 67 \times 0 $''$ 42	0.12	...
Per-emb 37		03:29:18.97	31:23:14.28	7.5	0 $''$ 67 \times 0 $''$ 42	0 $''$ 82 \times 0 $''$ 57	0.56	Y20
Per-emb 60		03:29:20.05	31:24:07.35	...	0 $''$ 67 \times 0 $''$ 42	0 $''$ 73 \times 0 $''$ 47	0.08	...
Per-emb 5	IRAS 03282+3035	03:31:20.94	30:45:30.24	7.3	0 $''$ 45 \times 0 $''$ 30	0 $''$ 56 \times 0 $''$ 41	15.29	S19
Per-emb 2	IRAS 03292+3039	03:32:17.92	30:49:47.81	7.0	0 $''$ 45 \times 0 $''$ 30	1 $''$ 35 \times 0 $''$ 97	7.41	S19
Per-emb 10	B1-d	03:33:16.43	31:06:52.01	6.4	0 $''$ 46 \times 0 $''$ 30	0 $''$ 49 \times 0 $''$ 32	1.82	S19
Per-emb 40	B1-a	03:33:16.67	31:07:54.87	7.4	0 $''$ 46 \times 0 $''$ 30	0 $''$ 47 \times 0 $''$ 32	1.44	S19
Per-emb 29	B1-c	03:33:17.88	31:09:31.74	6.1	0 $''$ 46 \times 0 $''$ 30	0 $''$ 56 \times 0 $''$ 39	8.41	Y20
B1-b N		03:33:21.21	31:07:43.63	6.6	0 $''$ 46 \times 0 $''$ 30	0 $''$ 56 \times 0 $''$ 47	7.67	C16
B1-b S		03:33:21.36	31:07:26.34	6.6	0 $''$ 46 \times 0 $''$ 30	0 $''$ 63 \times 0 $''$ 53	14.79	C16
Per-emb 16		03:43:50.97	32:03:24.12	8.8	0 $''$ 50 \times 0 $''$ 32	0 $''$ 61 \times 0 $''$ 52	0.35	S19
Per-emb 28		03:43:51.01	32:03:08.02	8.6	0 $''$ 50 \times 0 $''$ 32	0 $''$ 56 \times 0 $''$ 32	1.52	S19
Per-emb 1	HH 211 MMS	03:43:56.81	32:00:50.16	9.4	0 $''$ 49 \times 0 $''$ 32	0 $''$ 68 \times 0 $''$ 48	4.57	S19
Per-emb 11 B	IC 348 MMS	03:43:56.88	32:03:03.08	9.0	0 $''$ 50 \times 0 $''$ 33	0 $''$ 92 \times 0 $''$ 69	0.40	S19
Per-emb 11 A	IC 348 MMS	03:43:57.07	32:03:04.76	9.0	0 $''$ 50 \times 0 $''$ 33	0 $''$ 61 \times 0 $''$ 48	10.47	S19
Per-emb 11 C	IC 348 MMS	03:43:57.70	32:03:09.82	9.0	0 $''$ 50 \times 0 $''$ 33	1 $''$ 10 \times 0 $''$ 86	0.34	S19
Per-emb 55	IRAS 03415+3152	03:44:43.30	32:01:31.22	12.0	0 $''$ 50 \times 0 $''$ 32	0 $''$ 49 \times 0 $''$ 33	0.32	S19
Per-emb 8		03:44:43.98	32:01:35.19	11.0	0 $''$ 50 \times 0 $''$ 32	0 $''$ 49 \times 0 $''$ 36	8.51	S19
Per-emb 53	B5 IRS 1	03:47:41.59	32:51:43.62	10.2	0 $''$ 51 \times 0 $''$ 33	0 $''$ 58 \times 0 $''$ 42	1.55	Y20

References—C16=Carney et al. (2016); H18=Higuchi et al. (2018); S18=Stephens et al. (2018); S19=Stephens et al. (2019); Y20=this study.

Table 2. PEACHES Sample

PEACHES ID	Source	Common names	R.A. (J2000)	Decl. (J2000)	v_{lsr}	Beam	Cont. Size	T_{cont}	Ref. (v_{lsr})
			(hh:mm:ss)	(dd:mm:ss)	(km s ⁻¹)	($''$)	($''$)	(K)	
Set1_ID00	L1448 NW	L1448 IRS 3C	03:25:35.67	30:45:34.16	4.2	0 $''$ 64×0 $''$ 39	0 $''$ 83×0 $''$ 47	3.15	H18
Set1_ID01.3	Per-emb 33 A		03:25:36.38	30:45:14.72	5.3	0 $''$ 64×0 $''$ 39	0 $''$ 73×0 $''$ 45	10.33	S19
Set1_ID01.4	Per-emb 33 B/C		03:25:36.32	30:45:15.19	5.3	0 $''$ 64×0 $''$ 39	0 $''$ 75×0 $''$ 48	5.55	S19
Set1_ID01.2	L1448 IRS 3A		03:25:36.50	30:45:21.90	4.6	0 $''$ 64×0 $''$ 39	0 $''$ 85×0 $''$ 59	3.21	H18
Set1_ID02	Per-emb 26		03:25:38.88	30:44:05.28	5.4	0 $''$ 64×0 $''$ 39	0 $''$ 69×0 $''$ 45	8.03	S19
Set1_ID02.2	Per-emb 42		03:25:39.14	30:43:57.90	5.8	0 $''$ 64×0 $''$ 39	0 $''$ 64×0 $''$ 39	0.66	S19
Set1_ID03	Per-emb 22 A		03:25:22.41	30:45:13.26	4.3	0 $''$ 64×0 $''$ 39	0 $''$ 86×0 $''$ 65	1.71	S19
Set1_ID03.2	Per-emb 22 B		03:25:22.35	30:45:13.11	4.3	0 $''$ 64×0 $''$ 39	0 $''$ 95×0 $''$ 51	0.92	S19
Set1_ID05	Per-emb 25	IRAS 03235+3004	03:26:37.51	30:15:27.81	5.5	0 $''$ 64×0 $''$ 39	0 $''$ 69×0 $''$ 41	5.27	S18
Set1_ID06	Per-emb 17	L1455 IRS 1, IRAS 03245+3002	03:27:39.11	30:13:02.96	6.0	0 $''$ 64×0 $''$ 40	0 $''$ 79×0 $''$ 48	2.00	S19
Set1_ID07	Per-emb 20	L1455 IRS 4	03:27:43.28	30:12:28.88	5.3	0 $''$ 64×0 $''$ 40	1 $''$ 29×0 $''$ 78	0.14	S19
Set1_ID08	L1455 IRS 2		03:27:47.69	30:12:04.33	5.1	0 $''$ 64×0 $''$ 40	0 $''$ 60×0 $''$ 38	0.13	H18
Set2_ID00	Per-emb 44	NGC 1333 SVS 13A	03:29:03.76	31:16:03.70	8.7	0 $''$ 66×0 $''$ 42	0 $''$ 98×0 $''$ 79	6.84	S19
Set2_ID00.2	SVS 13A2	VLA 3	03:29:03.39	31:16:01.58	8.4	0 $''$ 66×0 $''$ 42	0 $''$ 86×0 $''$ 53	0.61	S18
Set2_ID01	Per-emb 12 A	NGC 1333 IRAS 4A1	03:29:10.54	31:13:30.93	6.9	0 $''$ 66×0 $''$ 42	1 $''$ 11×0 $''$ 98	21.85	S19
Set2_ID01.2	Per-emb 12 B	NGC 1333 IRAS 4A2	03:29:10.44	31:13:32.08	6.9	0 $''$ 66×0 $''$ 42	1 $''$ 33×0 $''$ 81	10.04	S19
Set2_ID02	Per-emb 13	NGC 1333 IRAS 4B1	03:29:12.02	31:13:07.99	7.1	0 $''$ 66×0 $''$ 42	1 $''$ 07×0 $''$ 83	14.76	S19
Set2_ID02.2	IRAS4B'	NGC 1333 IRAS 4B2	03:29:12.85	31:13:06.87	7.1	0 $''$ 66×0 $''$ 42	0 $''$ 83×0 $''$ 74	7.13	S19
Set2_ID03	Per-emb 27	NGC 1333 IRAS 2A	03:28:55.57	31:14:36.97	6.5	0 $''$ 66×0 $''$ 42	0 $''$ 93×0 $''$ 66	5.79	Y20
Set2_ID04	Per-emb 54	NGC 1333 IRAS 6	03:29:01.55	31:20:20.49	7.9	0 $''$ 66×0 $''$ 42	0 $''$ 69×0 $''$ 40	0.07	S19
Set2_ID05	Per-emb 21	NGC 1333 IRAS 7 SM2	03:29:10.67	31:18:20.16	8.6	0 $''$ 66×0 $''$ 42	0 $''$ 74×0 $''$ 48	2.05	Y20
Set2_ID06	Per-emb 14	NGC 1333 IRAS 4C	03:29:13.55	31:13:58.12	7.9	0 $''$ 66×0 $''$ 42	0 $''$ 79×0 $''$ 50	3.05	S19
Set2_ID07	Per-emb 35 A	NGC 1333 IRAS 1	03:28:37.10	31:13:30.77	7.4	0 $''$ 66×0 $''$ 42	0 $''$ 75×0 $''$ 51	0.93	Y20
Set2_ID07.2	Per-emb 35 B	NGC 1333 IRAS 1	03:28:37.22	31:13:31.74	7.3	0 $''$ 66×0 $''$ 42	0 $''$ 78×0 $''$ 53	0.75	Y20
Set2_ID08	SVS 13B	NGC 1333 SVS 13B	03:29:03.08	31:15:51.73	8.5	0 $''$ 66×0 $''$ 42	0 $''$ 87×0 $''$ 68	6.64	S19
Set2_ID09	Per-emb 15		03:29:04.06	31:14:46.23	6.8	0 $''$ 66×0 $''$ 42	0 $''$ 89×0 $''$ 70	0.17	S19
Set2_ID11	Per-emb 50	IRAS 03260+3111 A	03:29:07.77	31:21:57.11	9.3	0 $''$ 66×0 $''$ 42	0 $''$ 73×0 $''$ 44	4.13	Y20
Set2_ID12	Per-emb 18	NGC 1333 IRAS 7 SM1	03:29:11.27	31:18:31.09	8.1	0 $''$ 66×0 $''$ 42	0 $''$ 84×0 $''$ 73	3.42	S19
Set2_ID13	Per-emb 37		03:29:18.97	31:23:14.28	7.5	0 $''$ 67×0 $''$ 42	0 $''$ 82×0 $''$ 57	0.56	Y20
Set2_ID13.2	EDJ2009-235		03:29:18.26	31:23:19.73	7.7	0 $''$ 67×0 $''$ 42	0 $''$ 66×0 $''$ 44	0.26	Y20
Set2_ID13.3	EDJ2009-237		03:29:18.74	31:23:25.24	...	0 $''$ 67×0 $''$ 42	0 $''$ 67×0 $''$ 42	0.12	...
Set2_ID14	Per-emb 60		03:29:20.05	31:24:07.35	...	0 $''$ 67×0 $''$ 42	0 $''$ 73×0 $''$ 47	0.08	...
Set2_ID15	EDJ2009-172		03:28:56.65	31:18:35.43	...	0 $''$ 66×0 $''$ 42	0 $''$ 69×0 $''$ 44	0.62	...
Set2_ID16	Per-emb 36	NGC 1333 IRAS 2B	03:28:57.37	31:14:15.77	6.9	0 $''$ 66×0 $''$ 42	0 $''$ 73×0 $''$ 46	5.56	S19
Set3_ID00	B1-b S		03:33:21.36	31:07:26.34	6.6	0 $''$ 46×0 $''$ 30	0 $''$ 63×0 $''$ 53	14.79	C16
Set3_ID00.2	B1-b N		03:33:21.21	31:07:43.63	6.6	0 $''$ 46×0 $''$ 30	0 $''$ 56×0 $''$ 47	7.67	C16
Set3_ID01	Per-emb 29	B1-c	03:33:17.88	31:09:31.74	6.1	0 $''$ 46×0 $''$ 30	0 $''$ 56×0 $''$ 39	8.41	Y20
Set3_ID02	Per-emb 10	B1-d	03:33:16.43	31:06:52.01	6.4	0 $''$ 46×0 $''$ 30	0 $''$ 49×0 $''$ 32	1.82	S19
Set3_ID03	Per-emb 40	B1-a	03:33:16.67	31:07:54.87	7.4	0 $''$ 46×0 $''$ 30	0 $''$ 47×0 $''$ 32	1.44	S19
Set3_ID04	Per-emb 2	IRAS 03292+3039	03:32:17.92	30:49:47.81	7.0	0 $''$ 45×0 $''$ 30	1 $''$ 35×0 $''$ 97	7.41	S19
Set3_ID05	Per-emb 5	IRAS 03282+3035	03:31:20.94	30:45:30.24	7.3	0 $''$ 45×0 $''$ 30	0 $''$ 56×0 $''$ 41	15.29	S19
Set3_ID06	Per-emb 1	HH 211 MMS	03:43:56.81	32:00:50.16	9.4	0 $''$ 49×0 $''$ 32	0 $''$ 68×0 $''$ 48	4.57	S19
Set3_ID07	Per-emb 11 A	IC 348 MMS	03:43:57.07	32:03:04.76	9.0	0 $''$ 50×0 $''$ 33	0 $''$ 61×0 $''$ 48	10.47	S19
Set3_ID07.2	Per-emb 11 B	IC 348 MMS	03:43:56.88	32:03:03.08	9.0	0 $''$ 50×0 $''$ 33	0 $''$ 92×0 $''$ 69	0.40	S19
Set3_ID07.3	Per-emb 11 C	IC 348 MMS	03:43:57.70	32:03:09.82	9.0	0 $''$ 50×0 $''$ 33	1 $''$ 10×0 $''$ 86	0.34	S19
Set3_ID08	Per-emb 8		03:44:43.98	32:01:35.19	11.0	0 $''$ 50×0 $''$ 32	0 $''$ 49×0 $''$ 36	8.51	S19
Set3_ID08.2	Per-emb 55	IRAS 03415+3152	03:44:43.30	32:01:31.22	12.0	0 $''$ 50×0 $''$ 32	0 $''$ 49×0 $''$ 33	0.32	S19
Set3_ID09	Per-emb 16		03:43:50.97	32:03:24.12	8.8	0 $''$ 50×0 $''$ 32	0 $''$ 61×0 $''$ 52	0.35	S19
Set3_ID09.2	Per-emb 28		03:43:51.01	32:03:08.02	8.6	0 $''$ 50×0 $''$ 32	0 $''$ 56×0 $''$ 32	1.52	S19
Set3_ID10	Per-emb 53	B5 IRS 1	03:47:41.59	32:51:43.62	10.2	0 $''$ 51×0 $''$ 33	0 $''$ 58×0 $''$ 42	1.55	Y20

References—C16=Carney et al. (2016); H18=Higuchi et al. (2018); S18=Stephens et al. (2018); S19=Stephens et al. (2019); Y20=this study.

primary beam size (20''). For the field Set3_ID09, the fitting uses a threshold of 4σ and extends the mask to the entire primary beam as a continuum source is detected toward the edge of the primary beam where the noise is elevated.

- **Extracting spectra:** We use the CASA task `specflux` to extract the mean flux density within the ellipse which has the same major and minor axes as well as the position angle as the fitted continuum sources.
- **Baseline calibration:** The continuum has been removed before the imaging process; however, the extracted spectra sometimes still show imperfect baselines due to rich emission lines, lack of emission, and broad emission features. Thus, we manually select the frequency ranges for baseline calibration for each spectral window and each field.
- **Velocity correction:** Finally, the frequency of the extracted spectra are corrected according to the source velocities. We collect the source velocities from the literature as well as from the strong emission lines in our spectra, such as SO and CS. Table 1 lists the adopted source velocities and the corresponding references.

Figure 1 shows the continuum emission along with the fitted shapes, while the properties of the continuum sources are also listed in Table 1. Our observations detect 50 continuum sources. The continuum emission appears as compact circular or elliptical shape with no sub-structure. Some sources show extended continuum emission resembling the shape of outflow cavities, such as Per-emb 22 A and B. Three sources, EDJ2009-237, Per-emb 60, and EDJ2009-172, have no spectral line detected and no reliable measurement of source velocity in literature; therefore, we exclude them from spectral extraction as well as the line identification and modeling. However, these three sources still contribute to the denominator for calculating the detection statistics.

3.1. Line Identification and Modeling

Line identification starts with manual identification and verification for a few sources with rich spectra, including Per-emb-12B and B1-bS. We use SPLATALOGUE¹ to identify the molecular species and use XCLASS (Möller et al. 2017) to verify the identification. The XCLASS package is a LTE radiative transfer code that uses the molecular data from the Cologne Database of Molecular

Spectroscopy (CDMS; Müller et al. 2001, 2005; Endres et al. 2016) and the Jet Propulsion Laboratory (JPL; Pickett et al. 1998). An identification needs to satisfy the following criteria.

- The spectra agree with the predicted strengths of the model.
- The spectral lines are not all blended with other emission, such as other molecules and the SiO emission tracing the outflows. The emission of a few species, such as HDCO & ¹³CH₃OH, CH₃OH & CH₃OCHO, CH₃CHO & CH₂DOH, ³⁴SO & C₂H₅OH, and CH₃OCH₃ & CH₂DCN, are partially blended (blending occurs at a few lines but other lines remain isolated). The fittings of those species are performed together to verify their identification.
- Identified molecules need to be already found toward young stellar objects as summarized in McGuire (2018).

Table 4 lists the identified species and transitions that are detected in at least one of the PEACHES protostars. Only identifiable transitions are listed. The XCLASS modeling include all the transitions in our frequency coverage for each molecule regardless their Einstein-A values and upper energy levels.

Systematic spectral fitting using XCLASS is applied to all sources using a list of species, compiled from the identifications. Appendix A lists the catalogs used in this study. The fitting function in XCLASS includes several optimization algorithms that can be used in series to reduce biases. We configure the algorithm chain that starts with the genetic algorithm followed by the Levenberg-Marquardt χ^2 minimization. The genetic algorithm searches the best-fitting parameters iteratively with generations that evolve like a natural selection, where the better fitting models get less modification over generations. We setup the genetic algorithm to search for the top two best-fitting models with 30 generations. Then, the Levenberg-Marquardt χ^2 minimization applies to the two best-fitting models for 20 iterations to find the best-fitting models. The genetic algorithm aims to find local minimums and the Levenberg-Marquardt minimization further finds the best-fitting models in the local minimums. The two best-fitting models found by the genetic algorithm often very similar, suggesting that there is only one minimum. To address the rare cases of two separated local minimums, we pick the model with the lower χ^2 values from the two best-fitting models constrained by the Levenberg-Marquardt minimization.

¹ <http://www.splatalogue.net/>

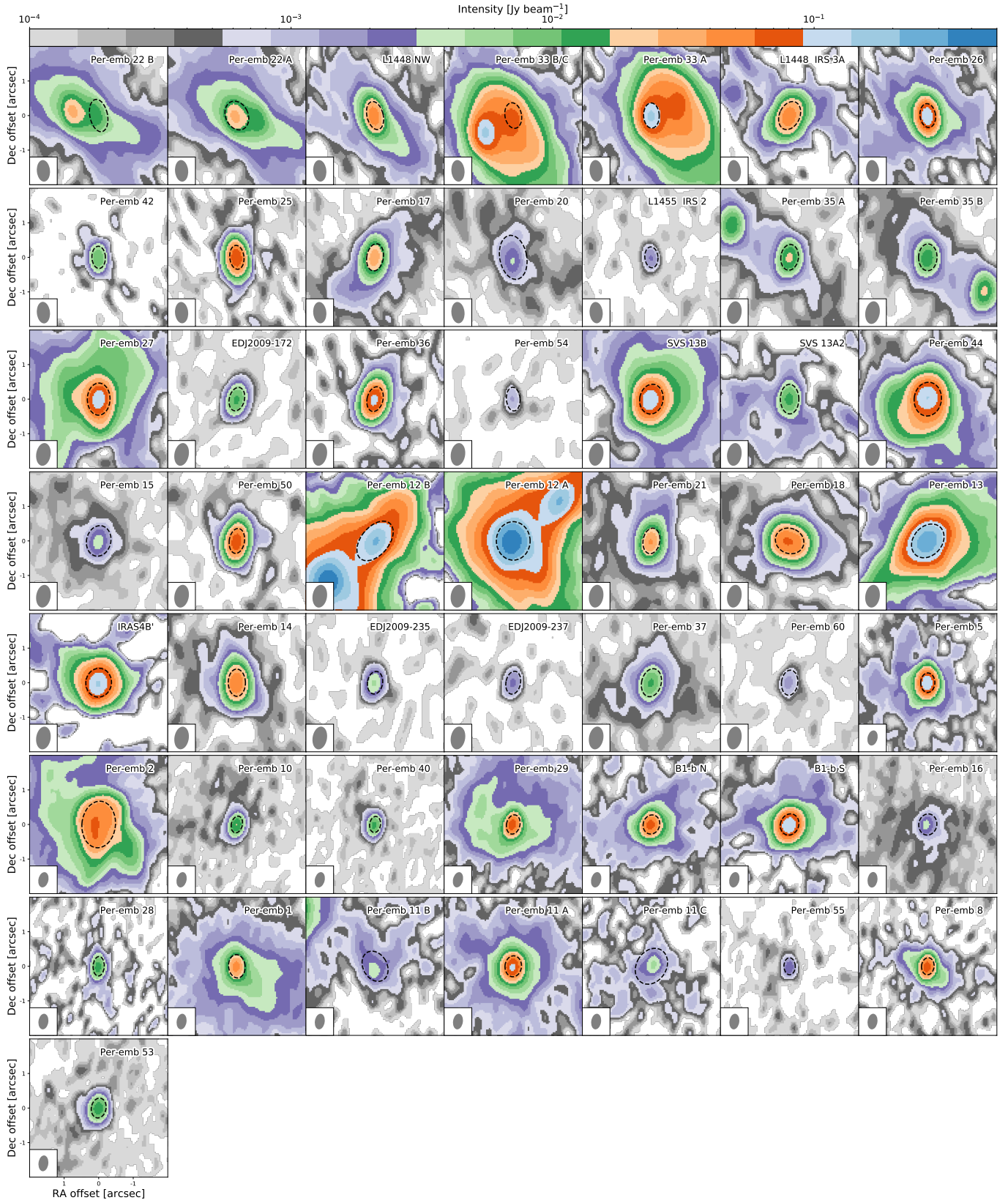


Figure 1. The continuum images of all PEACHES protostars. Non-detections toward L1448 IRS 2E and NGC 1333 SVS 3 are not shown. The dashed ellipses illustrate the size of fitted continuum, which is the region for extracting 1D spectra.

There are five parameters in the XCLASS modeling, the size of the emitting molecule (r_{COM}), the excitation temperature (T_{ex}), the column density (N_{COM}), the line width ($\Delta\nu$), and velocity offset (v_{off}). We assume the COMs are all concentrated at the center, simplified as a 2D thin circular disk. We fix r_{COM} as $0''.5$, similar to our beam size, and optimize the model with five excitation temperatures, 100, 150, 200, 250, and 300 K. We allow the line width varying between 1.2 km s^{-1} to 3.5 km s^{-1} for better fitting quality but assume no velocity offset from the source velocity, and the allowed range of the column density for each molecule is chosen according to the strength of the emission. From the fitting results of five T_{ex} , if a molecule is detected, the mean column densities will be the best-fitting column density, while the range of the column densities indicates the upper and lower uncertainties. If a molecule is non-detection, the synthetic spectra for all lines are scaled to match the peaks of the each line fitted by a Gaussian profile. Then, we take the minimum of the corresponding column densities as the upper limit.

4. DETECTION STATISTICS

We summarize the detection statistics in Figure 2, which includes COMs, the carbon-chain molecules, and the simple organic molecules, such as CS, H^{13}CN , SO, ^{34}SO , and SO_2 . In the following results of detection fraction, we include the three sources that are excluded from modeling due to no reliable source velocity, making a total of 50 sources. The PEACHES protostars show a great chemical diversity from no molecule detected (e.g., B1-bN and L1455 IRS 2) to rich spectra of COMs (e.g. Per-emb 13). Most of the PEACHES protostars have simple organics, such as SO, CS, H^{13}CN , and HDCO, and $\sim 60\%$ of sources have SO_2 and ^{34}SO . Emission of CCH can be easily identified from the spectra. However, the CCH toward the continuum sources often shows irregular line profiles together with velocity offsets and absorption (Figure 13). In fact, warm environments, such as the outflow cavity wall, easily enhance the abundance of CCH because of elevated abundance of C^+ . Thus, CCH emission is extended along with the outflow cavities, making the 1D spectra unrepresentative.

Thirty-four percent of sources have no COMs detected (no emission nor absorption), including Per-emb 8, B1-bN, IRAS 4B, Per-emb 36, Per-emb 33 B/C, Per-emb 50, Per-emb 14, Per-emb 28, Per-emb 41, Per-emb 37, Per-emb 11 B, Per-emb 16, Per-emb 55, EDJ2009-235, Per-emb 15, L1455 IRS 2, and Per-emb 54, in the order of decreasing continuum temperatures. Methanol (CH_3OH) is detected in 28 sources (56%); methyl for-

mate (CH_3OCHO) is detected in 15 sources (30%); and N-bearing COMs are detected in 20 sources (40%). Comparing to the COMs in the CALYPSO survey (Belloche et al. 2020), the fraction of sources that have methanol, $\sim 50\%$, is similar to that for the PEACHES protostars. Also, 30% of the CALYPSO sources have at least three COMs, while 28% of the PEACHES protostars have at least three COMs.

The sources with rich spectra COMs tend to have bright continuum emission. However, the brightest source in continuum, Per-emb 12 A has many molecules detected in absorption due to the high continuum opacity blocking the emission of COMs (Sahu et al. 2019). The number of detected COMs show no obvious correlation with the bolometric luminosity and bolometric temperature of the protostars (Figure 2), which are conventional evolutionary indicators. Low luminosity sources have fewer COMs detected; however, if COMs mostly come from thermal desorption, the region with $T > T_{\text{desorption}}$ may be smaller for the low luminosity sources, making the emission of COMs fainter and reducing our sensitivity to detect COMs. To test the detection statistics with physical properties of protostars, we collect the mass derived from 9 mm observations that resolved the sources as a proxy of the central mass (Tychoniec et al. 2018). The detection statistics with the continuum mass show only tentative correlation with the central mass with smaller central mass have fewer detections of COMs.

Several sources have their SiO emission with a broad line width, significantly contaminating the emission of $\text{CH}_3\text{CH}_2\text{CN}$ and CH_3CHO . In the later quantitative discussion, we exclude the spectral windows contaminated by the SiO emission. For assigning the detections, we can distinguish the emission of $\text{CH}_3\text{CH}_2\text{CN}$ and CH_3CHO from the broad SiO emission in a few sources, such as CH_3CHO in Per-emb 26.

5. CORRELATIONS OF COMS

The chemical evolution of protostars may leave certain patterns in the abundance of molecules as the dynamical evolution determines the density and temperature structures, which regulate chemical reactions. Thus, the abundance of COMs and their correlations provide critical information to constrain the chemical evolution at embedded protostars. The fitted column density of COMs indicates the abundance of COMs around protostars. Typically COMs are locked into the ices on dust grains at outer envelope. Therefore, we take the column density of COMs as a proxy of the abundance of COMs.

As described in Section 3.1, we fit the column density and line width with different excitation tempera-

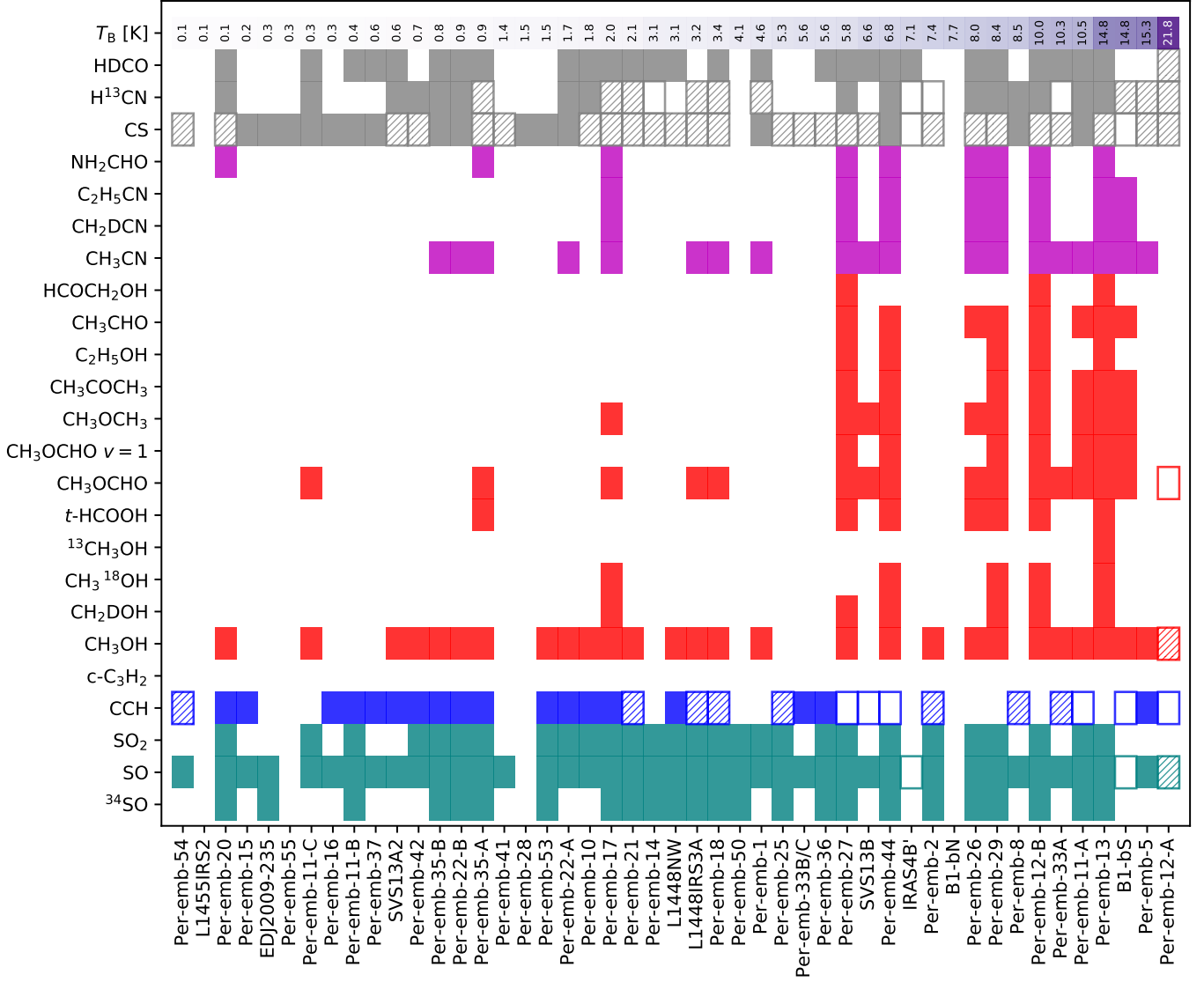


Figure 2. The same figure as Figure 2 but sorted by the continuum temperatures listed in Table 1.

tures, resulting in a range of column density as its uncertainty. The comparison between CCH and CH₃OH shows no correlation between these two molecules (Figure 12), similar to the conclusion in Higuchi et al. (2018). The single dish survey by Graninger et al. (2016) shows a correlation between C₄H, a more complex carbon-chain molecules, and CH₃OH. Outflow activity can promote the formation of CCH, which is more efficiency at warm temperature. In face, the morphology of CCH often traces the outflow cavities seen from CS. Therefore, the lack of correlation between CCH and CH₃OH may be affected by outflows.

Figure 5 shows the correlations of several COMs selected from their detection rates. The column density of CH₃OH best correlates with that of CH₃CN. Bellocche et al. (2020) also found the tight correlation be-

tween these two molecules from the CALYPSO survey, which has a selective sample. The column densities of CH₃OCH₃ and CH₃OCHO also show a tight correlation. To quantify the goodness of correlation, we calculate the Pearson’s correlation coefficient (r), which tests the linearity of two variables. A simple calculation of the Pearson’s correlation coefficient would ignore the uncertainties of the column density. Thus, we use the bootstrapping method to sample the fitted column densities to calculate Pearson’s r , by assuming a normal distribution centers on the best-fitted values with the uncertainty as the width of the normal distribution. If we include the upper limits as normal distributions center on zero, the correlation coefficient becomes significantly lower due to the cluster of samples around zero column density (Figure 4). With the detection-only sample, the mean Pear-

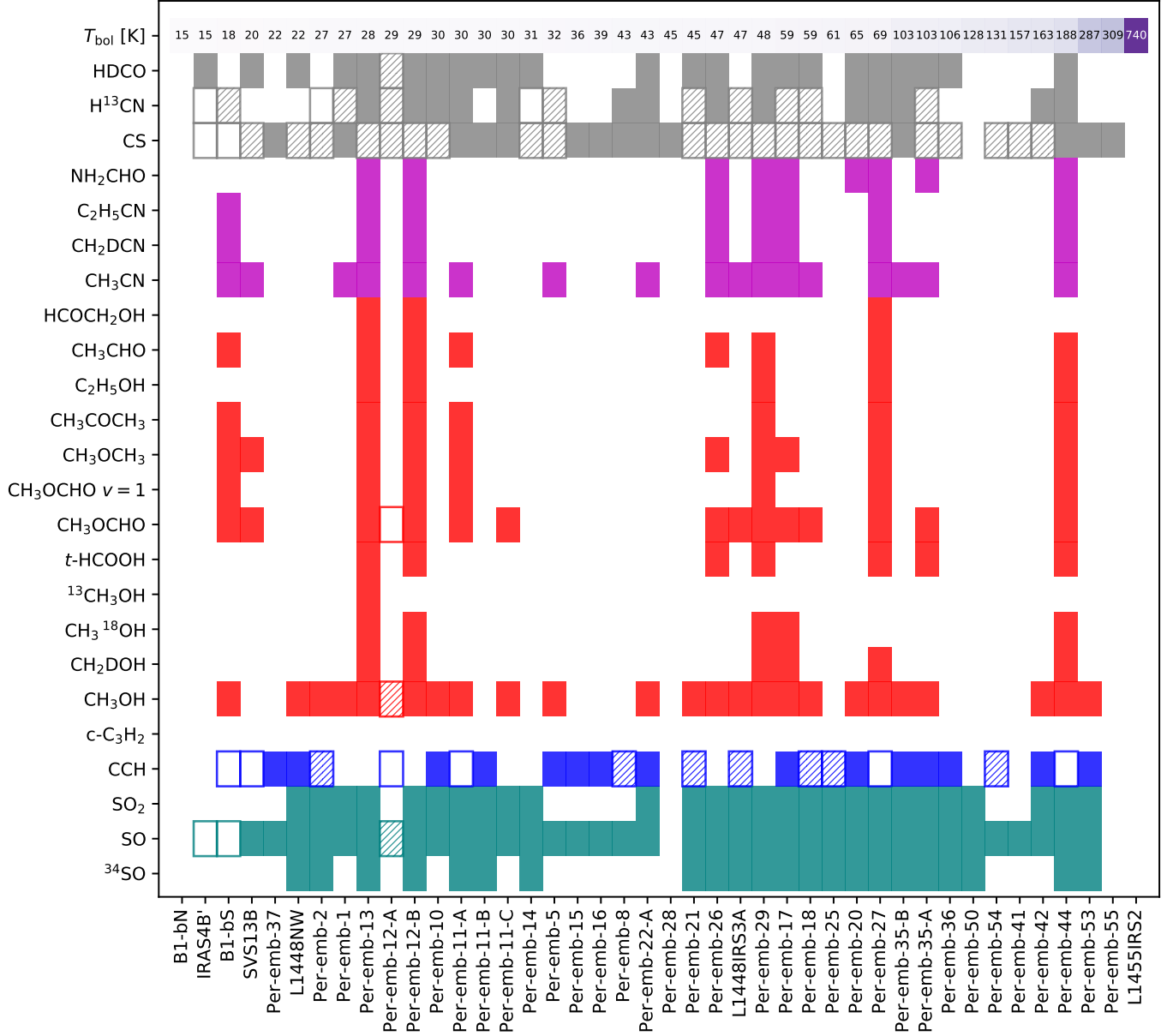


Figure 2 (Cont.). The same figure as Figure 2 but sorted by their bolometric temperature.

son's r_d is 0.91, as expected for a tight correlation, with a Gaussian-like distribution skewed toward lower values. After including the upper limits, the mean Pearson's r decreases to 0.59 with larger uncertainty (the 68% credible interval increases by 160%). Thus, the bootstrapped correlation coefficient only considers the detections.

5.1. Excitation Temperatures

5.1.1. CH_3OH

The PEACHES spectra cover four methanol lines, while the spectra of each source include three of them due to the frequency shift in the wide spectral window. The three methanol lines have upper energy rang-

ing from ~ 50 K to ~ 500 K, which allows us to estimate the rotational temperature of methanol if all three lines are detected. To construct the methanol rotational diagram, we fit the methanol emission with a Gaussian profile and bootstrap the measurements for fitting the rotational temperature. Figure 8 shows the rotational diagram of Per-emb 22 B along with the sampled rotational temperature. The derived rotational temperature of methanol ranges from 120 K to 240 K with an exception of Per-emb 18, which has a rotational temperature of 395.7 K for methanol (Table 3).

6. SPATIAL EXTENT OF COMS

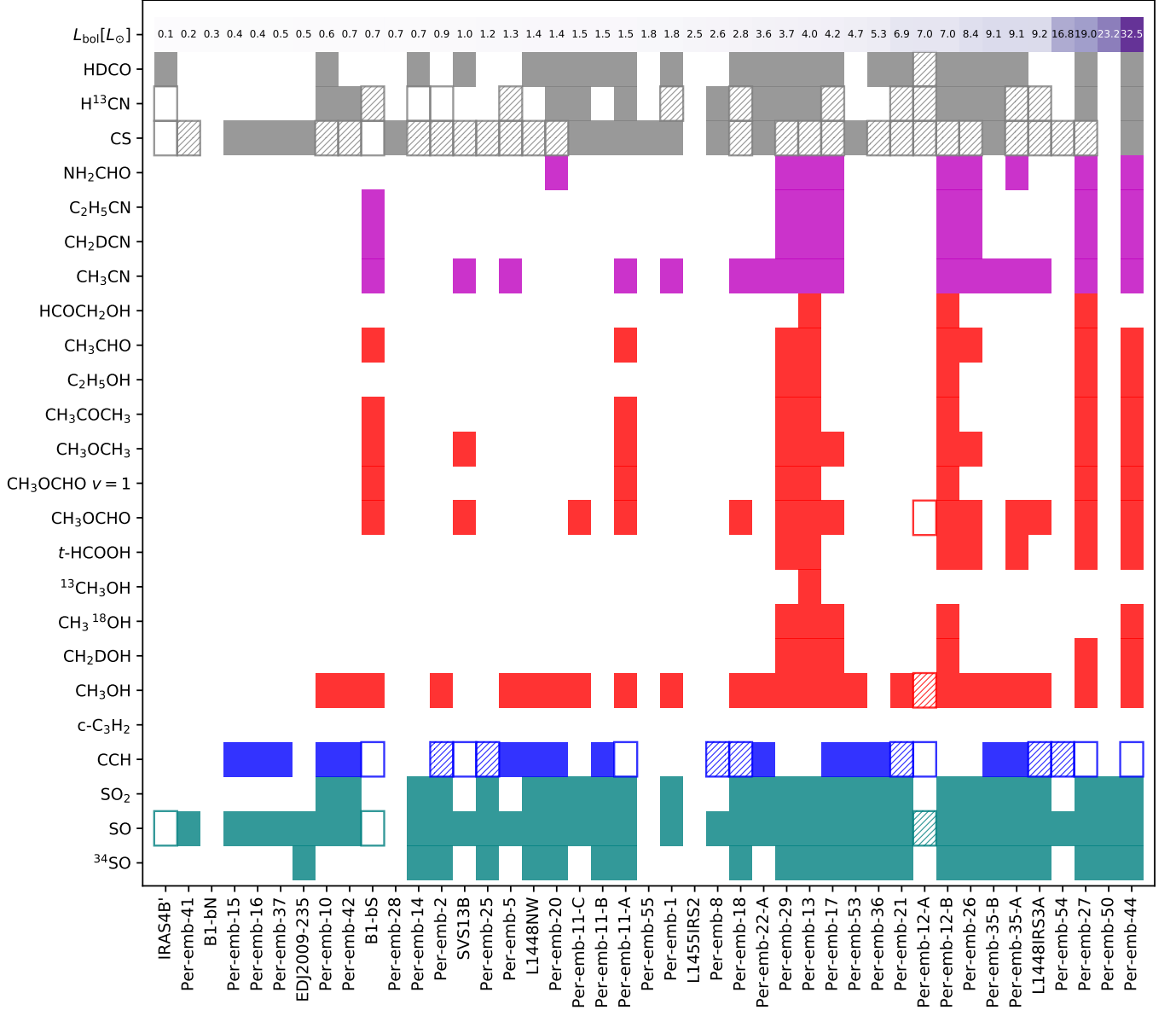


Figure 2 (Cont.). The detection statistics sorted by their bolometric luminosity.

7. DISCUSSION

7.1. Chemical Diversity in PEACHES

7.2. Comparison to Other Surveys

7.3. Complex Chemistry throughout Star Formation

7.4. 1D Spectra

Y.-L. Yang acknowledges the supports the JSPS Postdoctoral Fellowship from Japan Society for the Promotion of Science. This paper makes use of the following ALMA data: ADS/JAO.ALMA#2016.0.00391.S.

ALMA is a partnership of ESO (representing its member states), NSF (USA) and NINS (Japan), together with NRC (Canada), MOST and ASIAA (Taiwan), and KASI (Republic of Korea), in cooperation with the Republic of Chile. The Joint ALMA Observatory is operated by ESO, AUI/NRAO and NAOJ. The National Radio Astronomy Observatory is a facility of the National Science Foundation operated under cooperative agreement by Associated Universities, Inc.

Facilities: ALMA

Software: astropy, XCLASS, spectral-cube, CASA

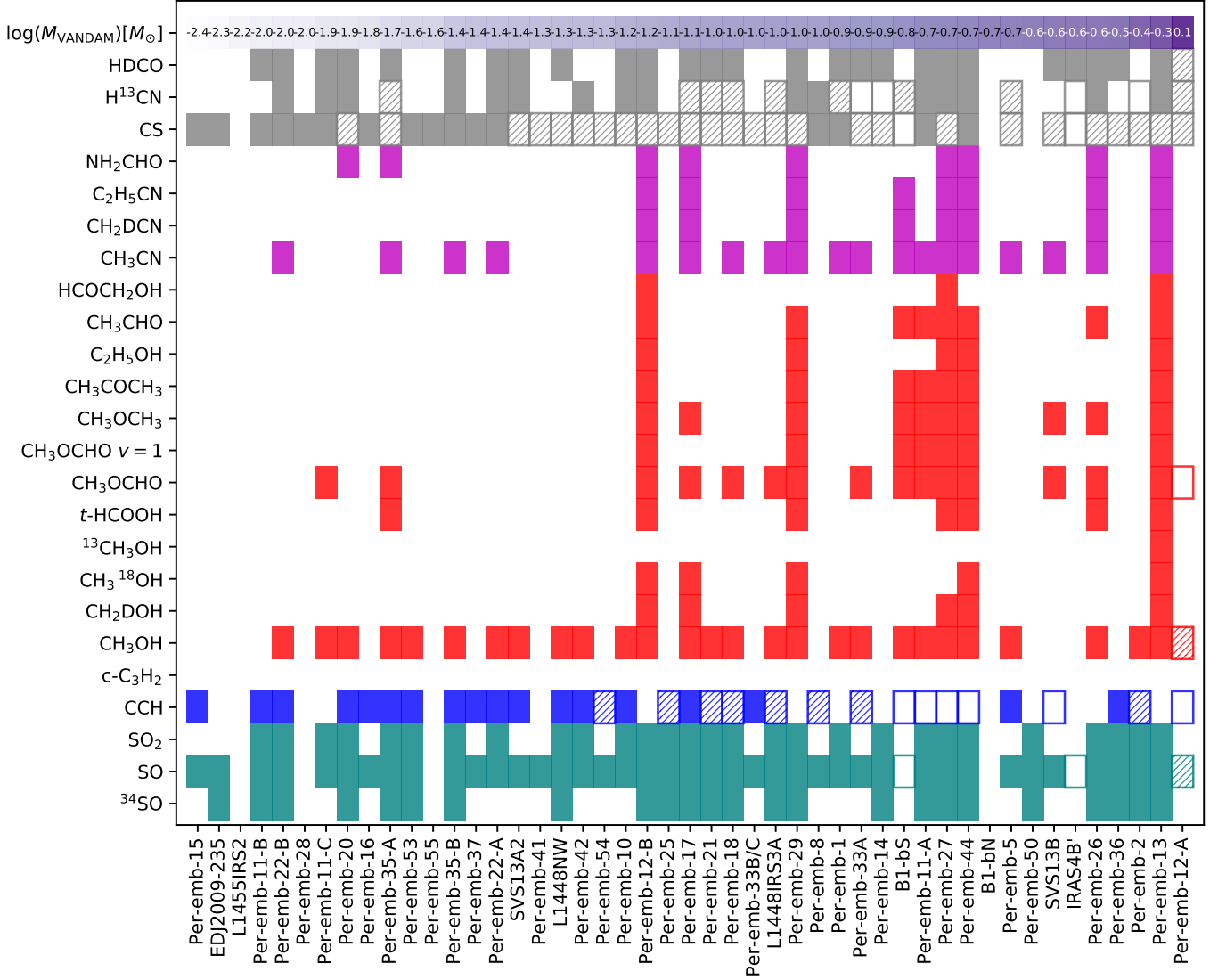


Figure 2 (Cont.). The same figure as Figure 2 but sorted by their mass derived from their 9 mm observations (Tychoniec et al. 2018).

APPENDIX

A. CATALOGS FOR MOLECULAR DATA

B. IDENTIFIED SPECIES AND TRANSITIONS

Table 4 lists the species and their transitions identified from the PEACHES spectra.

Table 4. Line Identification

Frequency (MHz)	Transition ^a	log(Einstein-A)	E_u (K)	g_u	Ref.
Ethyne (CCH)					
262065.00 (0.05)	[3, 5/2, 3]→[2, 3/2, 2] ^b	-4.31	25.16	7	CDMS

Table 4 continued

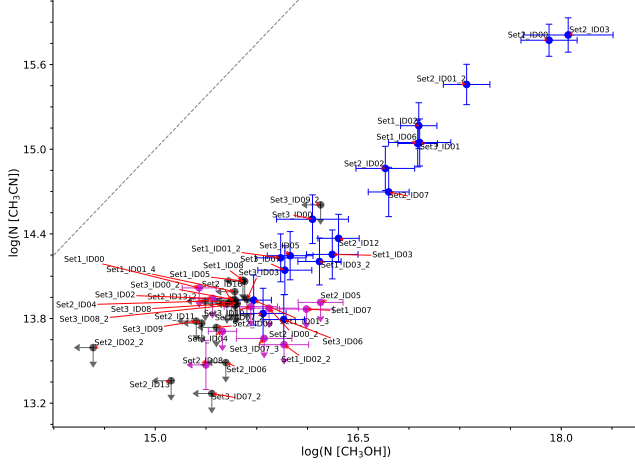


Figure 3. Correlation of the fitted column densities of CH_3OH and CH_3CN from the PEACHES protostars. The sources where both molecules are detected are shown in black; the sources where only one molecule is detected are shown in magenta; finally, the sources where both molecules are not detected are shown in black for the corresponding upper limits.

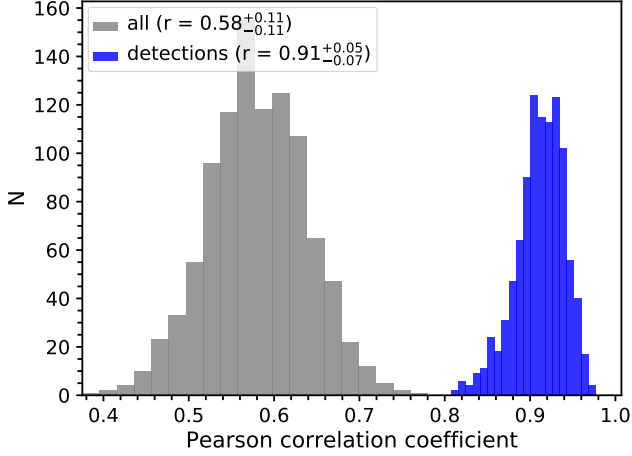


Figure 4. Distributions of Pearson's correlation coefficient from 10000 resamples drawn from detections + non-detections and only detections. The legend indicates the mean values of Pearson's r along with the range of the 95% credible interval as the associated uncertainties.

Table 4 (*continued*)

Frequency (MHz)	Transition ^a	log(Einstein-A)	E_u (K)	g_u	Ref.
262067.47 (0.05)	$[3, 5/2, 2] \rightarrow [2, 3/2, 1]^b$	-4.35	25.16	5	CDMS
262078.93 (0.02)	$[3, 5/2, 2] \rightarrow [2, 3/2, 2]^b$	-5.22	25.16	5	CDMS
Cyclopropenylidene ($\text{c-C}_3\text{H}_2$)					
244222.15 (0.01)	$[3, 2, 1] \rightarrow [2, 1, 2]$	-4.23	18.17	21	CDMS
246557.77 (0.02)	$[16, 10, 7] \rightarrow [16, 9, 8]$	-3.36	397.83	99	CDMS
260479.75 (0.02)	$[5, 3, 2] \rightarrow [4, 4, 1]$	-3.79	44.72	33	CDMS

Table 4 continued

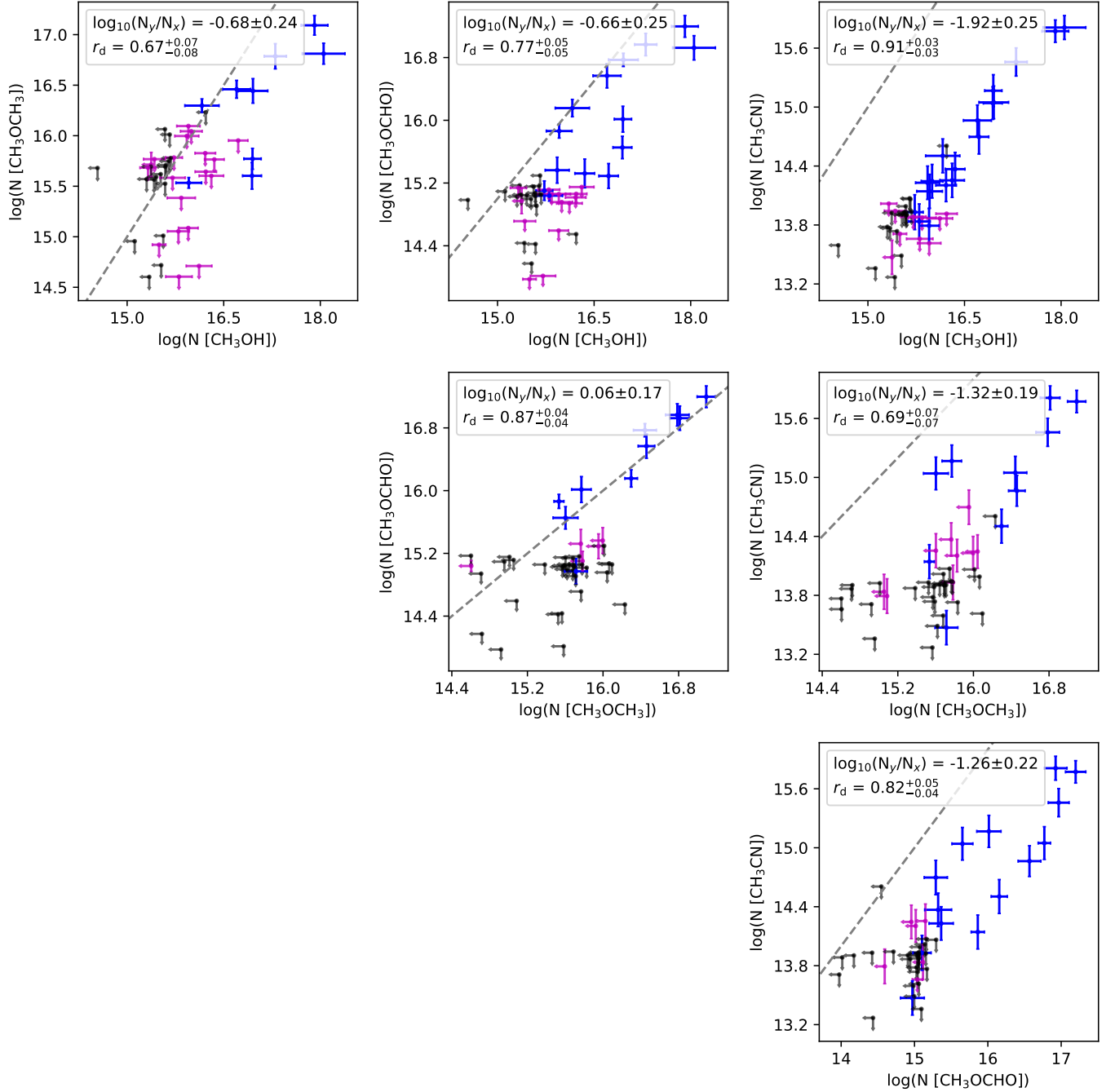


Figure 5. Corner plot of the correlations of the column densities between CH_3OH , CH_3CN , CH_3OCHO , and CH_3OCH_3 . The color code follows that in Figure 3. The dashed line indicates equality. The legends indicate the Pearson's r for the detection-only sample (r_d) and the logarithmic ratio of the two molecules (N_y/N_x). The four most detected COMs are shown in this figure, while other COMs are shown in Figure 7.

Table 4 (*continued*)

Frequency (MHz)	Transition ^a	$\log(\text{Einstein-A})$	E_u (K)	g_u	Ref.
Methanol (CH_3OH $v_t = 0$)					
243915.79 (0.01)	$[5, 1, 4] \rightarrow [4, 1, 3]$ A	-4.22	49.66	44	CDMS

Table 4 *continued*

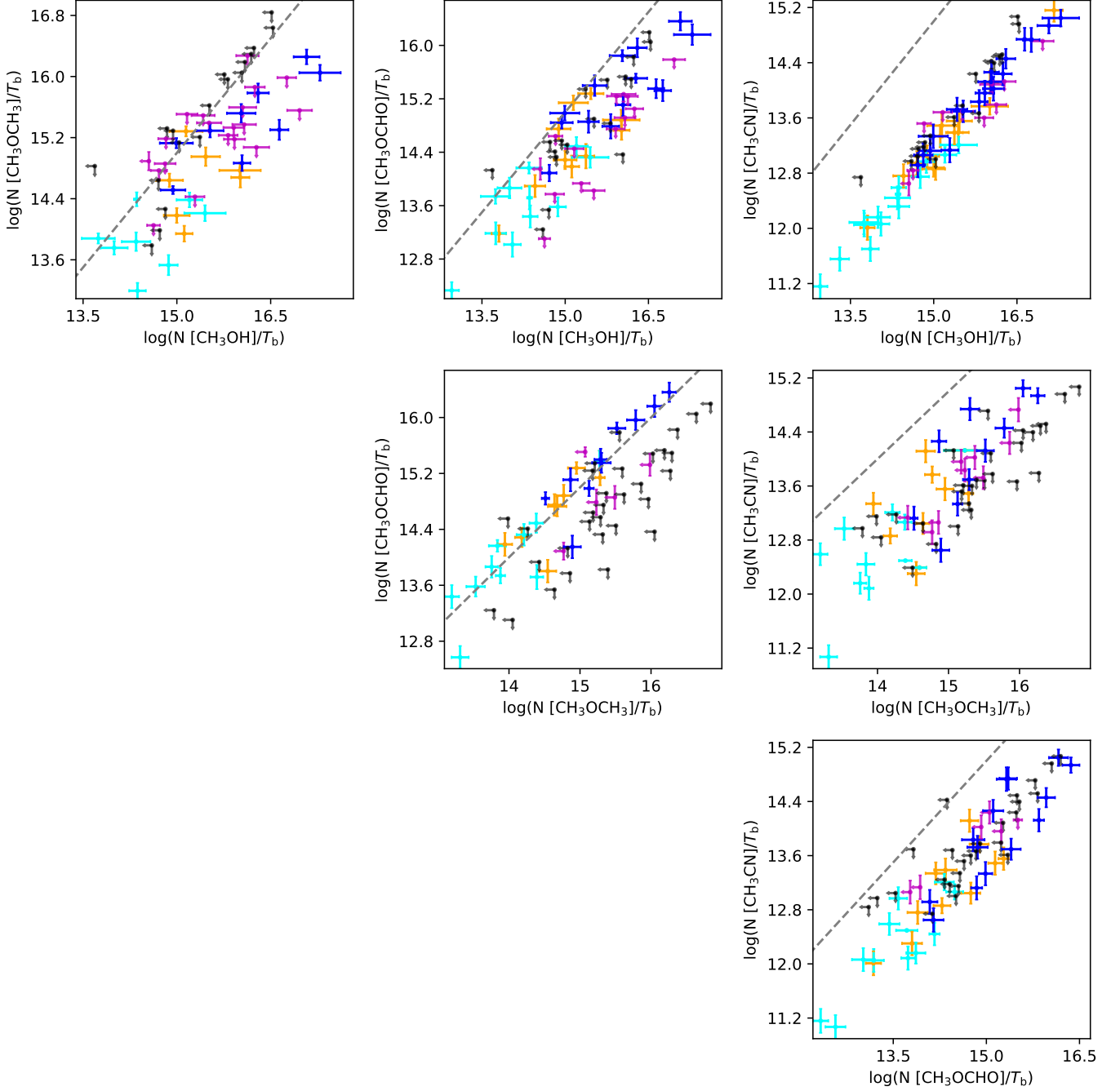


Figure 6. Corner plot of the correlations of the normalized column densities. The blue, magenta, and black symbols indicate the column densities normalized by the continuum brightness temperature (T_b), while the color scheme follows that in Figure 3. The orange symbols show the column densities normalized by T_b and the bolometric luminosity (L_{bol}), while the cyan symbols show that normalized by T_b and the bolometric temperature (T_{bol}). We only show the column densities if both molecules are detected for the ones normalized by $T_b T_{bol}$ and $T_b L_{bol}$. A few close multiple sources, including Per-emb 12 A & B, Per-emb 35 A & B, and Per-emb 11 A & C, are excluded for the normalization of T_{bol} and L_{bol} due to their poorly determined SEDs.

Table 4 continued

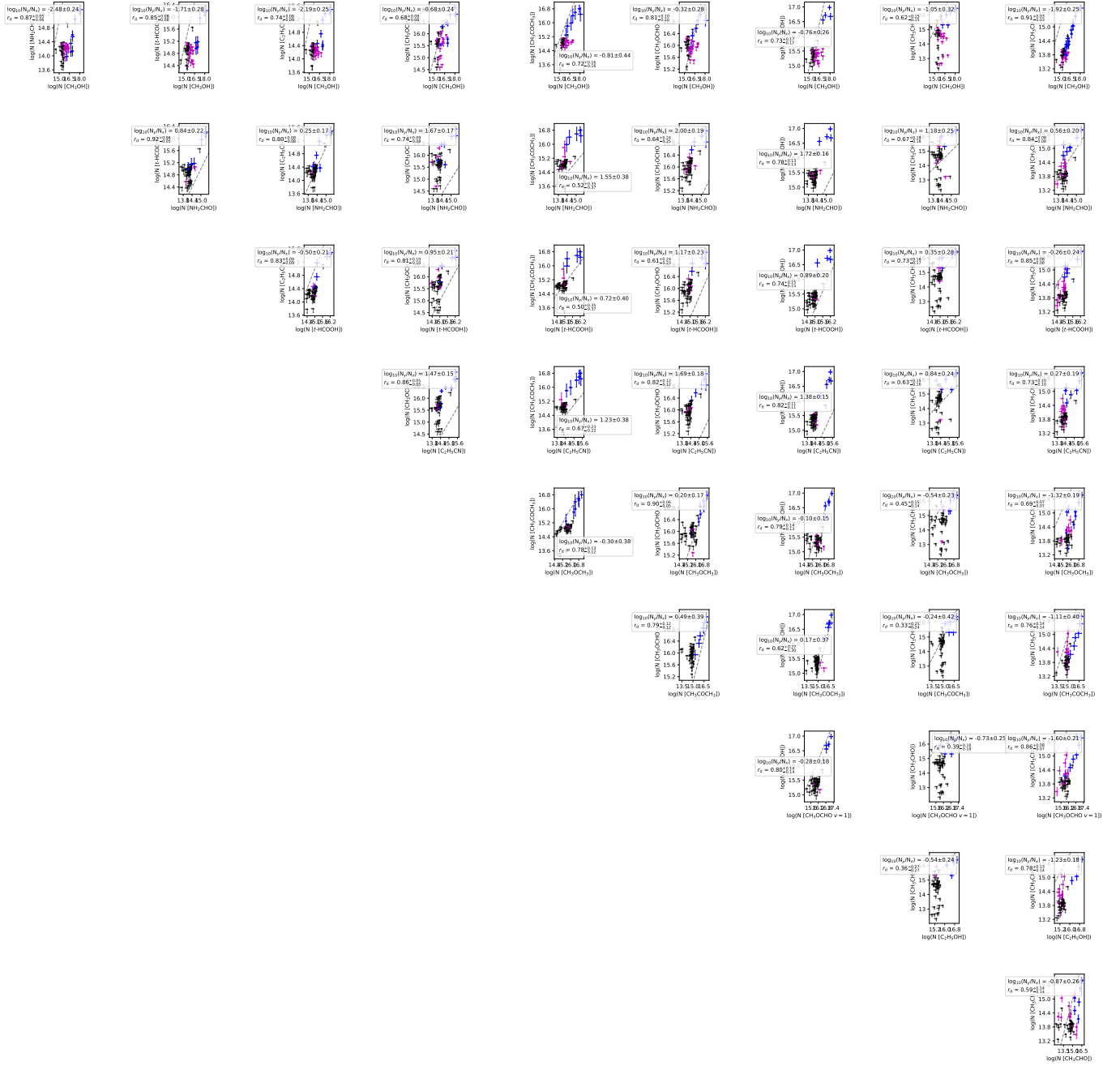


Figure 7. Corner plot of the correlations of the column densities between CH_3OH , CH_3CN , CH_3CHO , $\text{C}_2\text{H}_5\text{OH}$, $\text{CH}_3\text{OCHO } v = 1$, CH_3COCH_3 , $\text{CH}_3\text{CH}_2\text{CN}$, $t\text{-HCOOH}$, and NH_2CHO . The legends are similar to Figure 3

Table 4 (*continued*)

Frequency (MHz)	Transition ^a	log(Einstein-A)	E_u (K)	g_u	Ref.
Table 4 (<i>continued</i>)					
Frequency (MHz)	Transition ^a	log(Einstein-A)	E_u (K)	g_u	Ref.
246074.61 (0.02)	[20, 3, 17]→[20, 2, 18] A	−4.08	537.03	164	CDMS
246873.30 (0.02)	[19, 3, 16]→[19, 2, 17] A	−4.08	490.65	156	CDMS
261805.68 (0.01)	[2, 1, 1]→[1, 0, 1] E	−4.25	28.01	20	CDMS

Table 4 continued

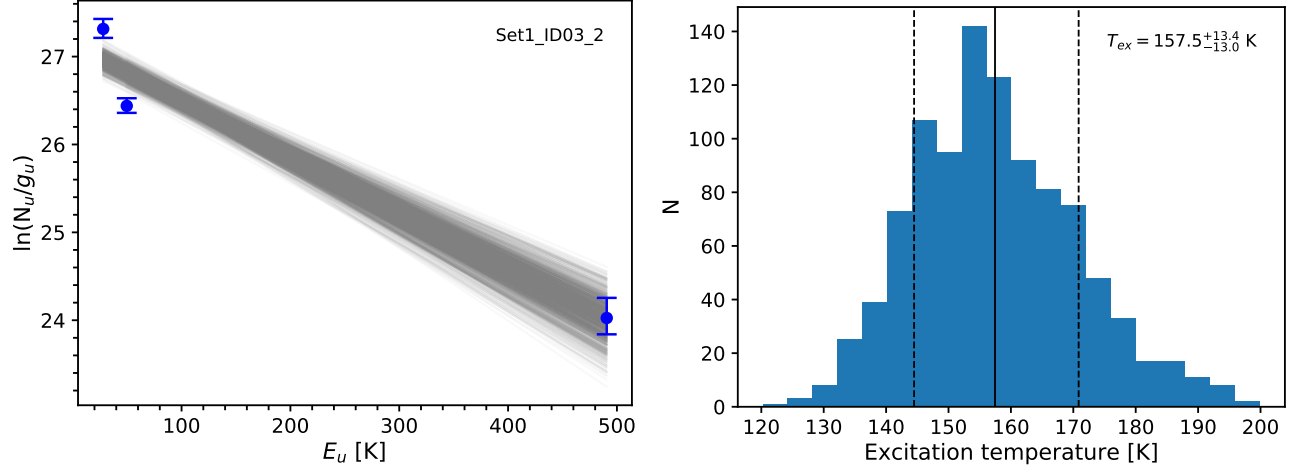


Figure 8. The methanol rotational diagram for Per-emb 22B and the fitted excitation temperature distribution using the bootstrapping method.

Table 3. Rotational Temperatures of Methanol

Source	T_{rot}
Per-emb 26	$120.1^{+2.6}_{-2.5}$ K
Per-emb 22 A	$182.4^{+11.2}_{-11.4}$ K
Per-emb 22 B	$157.5^{+13.4}_{-13.0}$ K
Per-emb 17	$173.9^{+1.8}_{-1.9}$ K
Per-emb 44	$197.5^{+0.3}_{-0.3}$ K
Per-emb 12 B	$194.0^{+0.8}_{-0.8}$ K
Per-emb 13	$208.6^{+3.9}_{-4.0}$ K
Per-emb 27	$195.8^{+0.4}_{-0.4}$ K
Per-emb 21	$151.0^{+14.6}_{-15.6}$ K
Per-emb 35 A	$145.1^{+3.7}_{-3.7}$ K
Per-emb 18	$395.7^{+30.7}_{-30.4}$ K
B1-bS	$241.7^{+11.7}_{-11.9}$ K
Per-emb 29	$227.7^{+3.2}_{-3.3}$ K

Table 4 (*continued*)

Frequency (MHz)	Transition ^a	log(Einstein-A)	E_u (K)	g_u	Ref.
Methanol ($^{13}\text{CH}_3\text{OH } v_t = 0$)					
246426.12 (0.22)	[23, 4, 19]→[22, 5, 18]	−4.58	721.02	47	CDMS
247086.3 (0.5)	[23, 3, 20]→[23, 2, 21] A−→ A+	−4.07	674.86	47	CDMS
259036.49 (0.17)	[17, 3, 15]→[17, 2, 16] A+→ A−	−4.04	396.48	35	CDMS
Methanol ($\text{CH}_2\text{DOH } v_t = 0$)					
243514.31 (0.01)	[9, 2, 8]→[10, 1, 10] o ₁	−5.17	131.85	19	JPL
246973.11 (0.01)	[4, 1, 4]→[4, 1, 3] e ₁	−4.67	37.69	9	JPL
260543.63 (0.01)	[3, 2, 1]→[3, 1, 2] o ₁	−4.65	48.34	7	JPL
Methanol ($\text{CH}_3^{18}\text{OH } v_t = 0$)					
246256.60 (0.04)	[11, 2, 10]→[10, 3, 7] A	−4.64	184.27	92	CDMS
Sulfur monoxide ($\text{SO } ^3\Sigma$)					
258255.83 (0.01)	[N, J]=[6, 6]→[5, 5]	−3.67	56.50	13	CDMS
261843.72 (0.03)	[N, J]=[7, 6]→[6, 5]	−3.64	47.55	15	CDMS

Table 4 continued

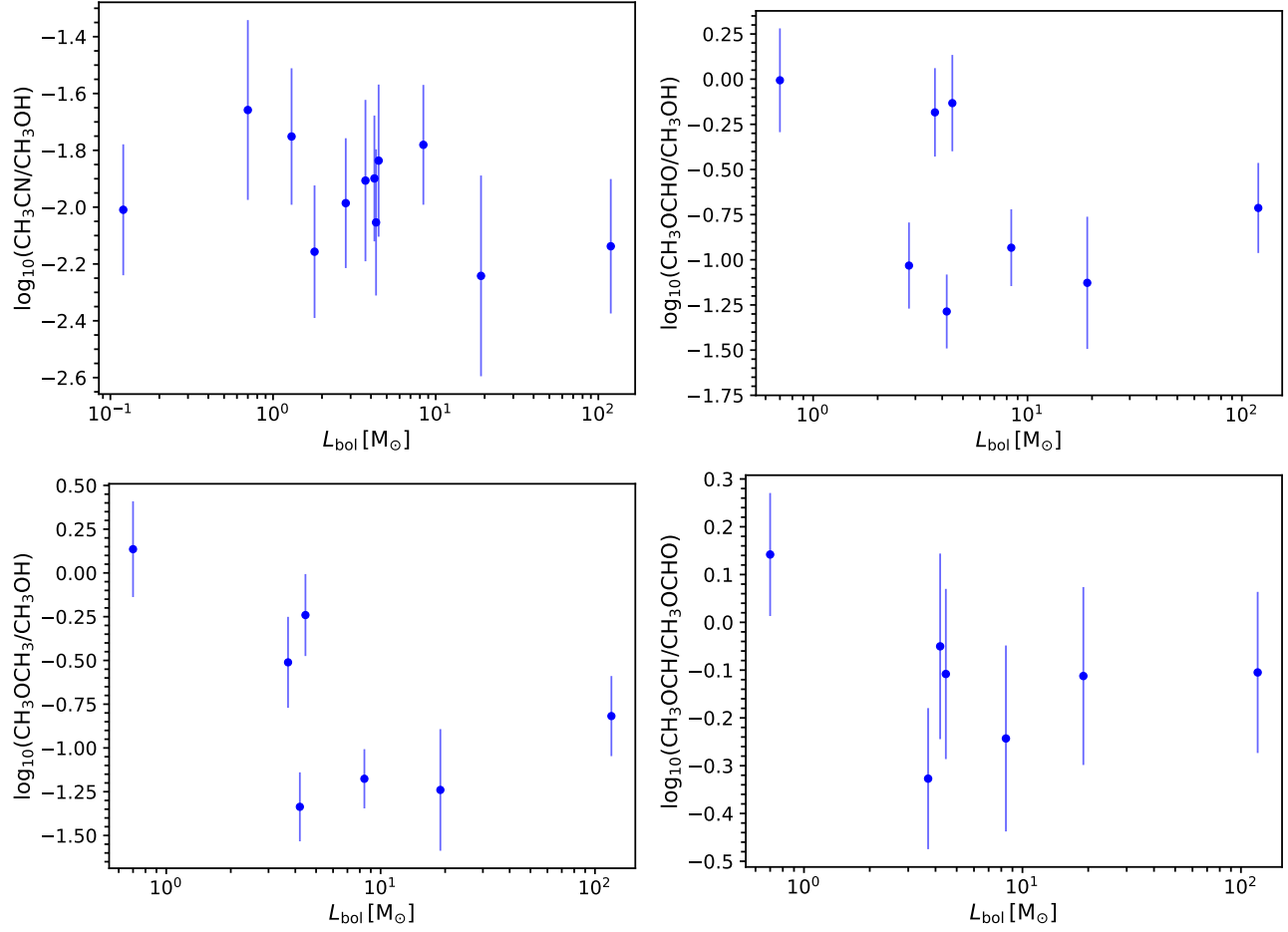


Figure 9. Ratios of molecules as a function of L_{bol} .

Table 4 (*continued*)

Frequency (MHz)	Transition ^a	log(Einstein-A)	E_u (K)	g_u	Ref.
Sulfur monoxide (^{34}SO)					
246663.47 (0.1)	$[N, J]=[5, 6] \rightarrow [4, 5]$	-3.74	49.89	11	CDMS
Sulfur dioxide (SO_2)					
244254.22 (0.01)	$[14, 0, 14] \rightarrow [13, 1, 13]$	-3.79	93.90	29	CDMS
Hydrogen cyanide (H^{13}CN)					
259010.26 (0.01)	$[J, F]=[3, 3] \rightarrow [2, 3]$	-4.07	24.86	7	CDMS
259011.55 (0.01)	$[J, F]=[3, 2] \rightarrow [2, 1]$	-3.19	24.86	5	CDMS
259011.80 (0.01)	$[J, F]=[3, 3] \rightarrow [2, 2]$	-3.16	24.86	7	CDMS
259011.86 (0.01)	$[J, F]=[3, 4] \rightarrow [2, 3]$	-3.11	24.86	9	CDMS
259012.34 (0.01)	$[J, F]=[3, 2] \rightarrow [2, 3]$	-5.46	24.86	5	CDMS
259013.89 (0.01)	$[J, F]=[3, 2] \rightarrow [2, 2]$	-3.92	24.86	5	CDMS
Carbon Monosulfide (CS)					
244935.56 (0.01)	$[J]=[5] \rightarrow [4]$	-3.53	35.27	11	CDMS
Formaldehyde (HDCO)					
246924.6 (0.1)	$[4, 1, 4] \rightarrow [3, 1, 3]$	-3.40	37.60	9	CDMS
259034.9 (0.1)	$[4, 2, 2] \rightarrow [3, 2, 1]$	-3.44	62.86	9	CDMS
Methyl formate (CH_3OCHO)					
245883.2 (0.1)	$[20, 13, 7] \rightarrow [19, 13, 6]$ E	-3.89	235.98	82	JPL
245885.2 (0.1)	$[20, 13, 7] \rightarrow [19, 13, 6]$ A	-3.89	235.98	82	JPL

Table 4 continued

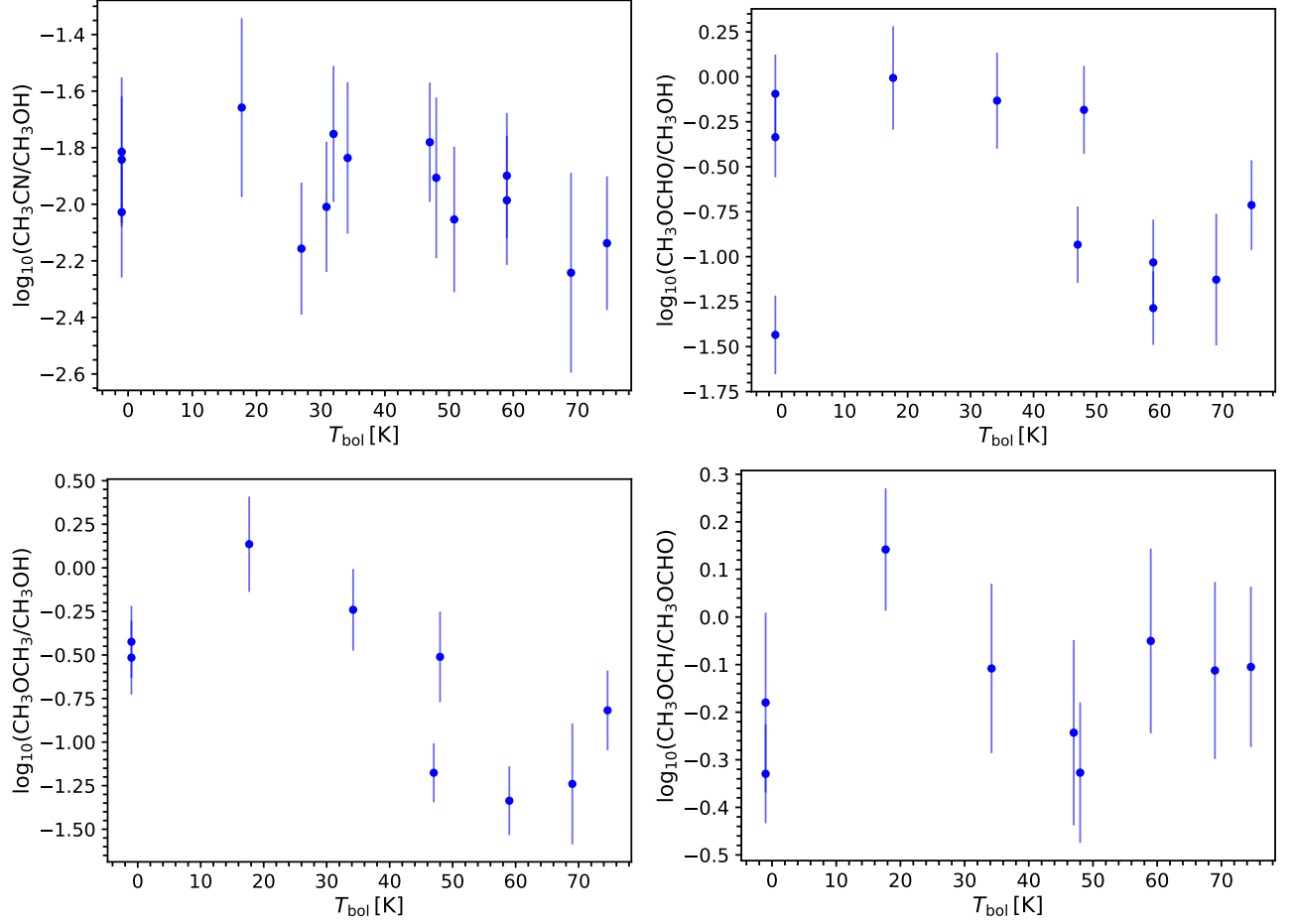
Figure 10. Ratios of molecules as a function of T_{bol} .

Table 4 (continued)

Frequency (MHz)	Transition ^a	log(Einstein-A)	E_u (K)	g_u	Ref.
245885.2 (0.1)	[20, 13, 8]→[19, 13, 7] A	−3.89	235.98	82	JPL
245903.7 (0.1)	[20, 13, 8]→[19, 13, 7] E	−3.89	235.97	82	JPL
246027.5 (0.1)	[21, 2, 19]→[20, 3, 18] E	−4.63	139.85	86	JPL
246038.9 (0.1)	[21, 2, 19]→[20, 3, 18] A	−4.63	139.85	86	JPL
246054.8 (0.1)	[20, 12, 8]→[19, 12, 7] E	−3.84	219.43	82	JPL
246060.8 (0.1)	[20, 12, 8/9]→[19, 12, 7/8] A	−3.84	219.43	82	JPL
246076.9 (0.1)	[20, 12, 9]→[19, 12, 8] E	−3.84	219.41	82	JPL
246285.4 (0.1)	[20, 11, 9]→[19, 11, 8] E	−3.80	204.21	82	JPL
246295.1 (0.1)	[20, 11, 10]→[19, 11, 9] A	−3.80	204.21	82	JPL
246295.1 (0.1)	[20, 11, 9]→[19, 11, 8] A	−3.80	204.21	82	JPL
246308.3 (0.1)	[20, 11, 10]→[19, 11, 9] E	−3.80	204.20	82	JPL
246456.1 (0.1)	[10, 5, 6]→[9, 4, 5] E	−5.52	49.09	42	JPL
246600.0 (0.1)	[20, 10, 10]→[19, 10, 9] E	−3.77	190.34	82	JPL
246613.4 (0.1)	[20, 10, 11]→[19, 10, 10] A	−3.77	190.34	82	JPL
246613.4 (0.1)	[20, 10, 10]→[19, 10, 9] A	−3.77	190.34	82	JPL
246623.2 (0.1)	[20, 10, 11]→[19, 10, 10] E	−3.77	190.34	82	JPL
246660.5 (0.1)	[10, 5, 6]→[9, 4, 5] A	−4.74	49.08	42	JPL
246675.4 (0.1)	[15, 4, 12]→[14, 3, 11] E	−4.93	81.85	62	JPL
246683.5 (0.1)	[15, 4, 12]→[14, 3, 11] A	−4.93	81.84	62	JPL

Table 4 continued

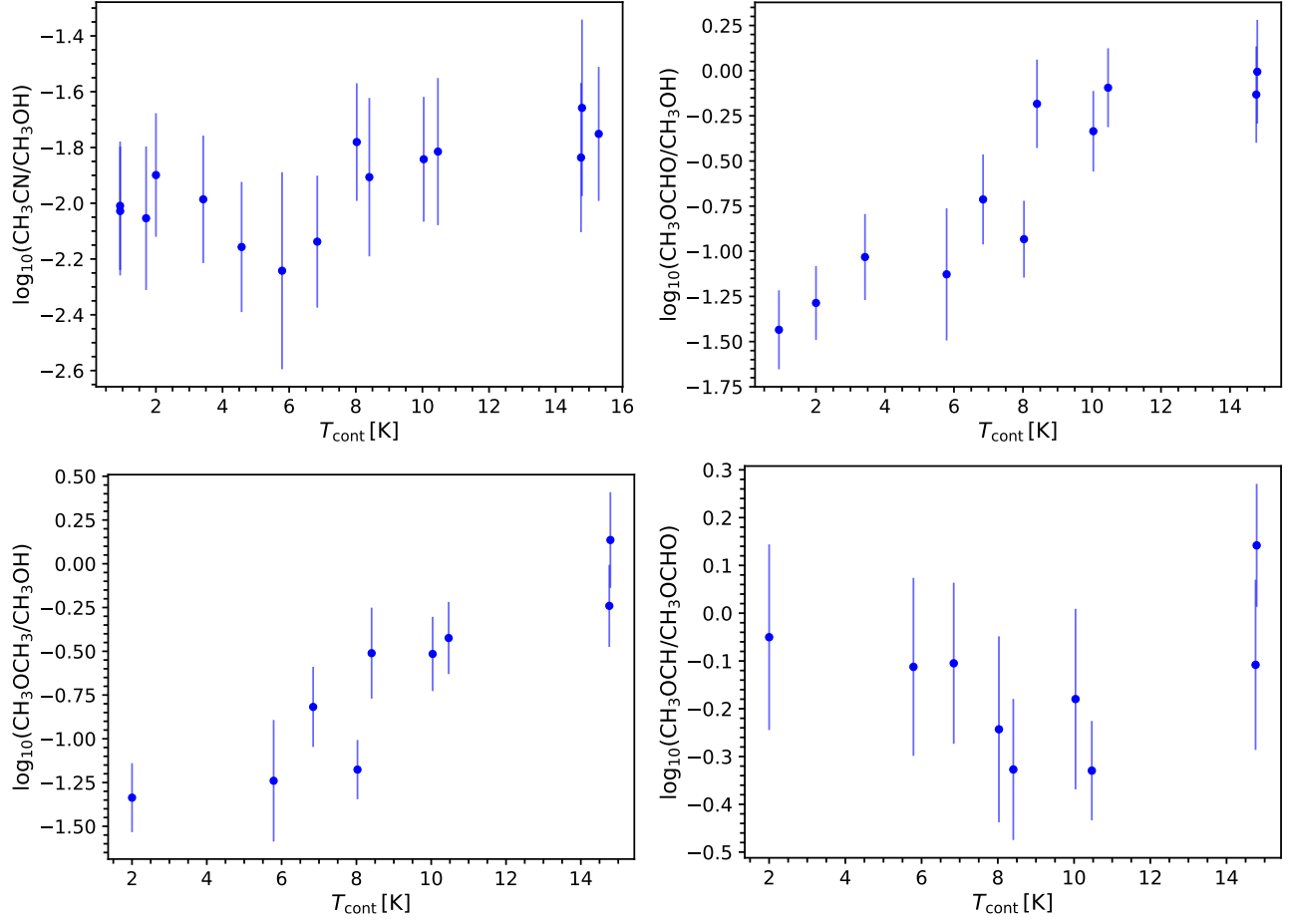


Figure 11. Ratios of molecules as a function of T_{cont} .

Table 4 (*continued*)

Frequency (MHz)	Transition ^a	log(Einstein-A)	E_u (K)	g_u	Ref.
246752.9 (0.1)	[10, 5, 5]→[9, 4, 5] E	-4.90	49.10	42	JPL
246891.6 (0.1)	[19, 4, 15]→[18, 4, 14] E	-3.66	126.22	78	JPL
246914.7 (0.1)	[19, 4, 15]→[18, 4, 14] A	-3.66	126.22	78	JPL
246945.7 (0.1)	[10, 5, 6]→[9, 4, 6] E	-4.90	49.09	42	JPL
247040.7 (0.1)	[20, 9, 11]→[19, 9, 10] E	-3.74	177.83	82	JPL
247044.1 (0.1)	[21, 3, 19]→[20, 3, 18] E	-3.66	139.90	86	JPL
247053.5 (0.1)	[21, 3, 19]→[20, 3, 18] A	-3.66	139.89	86	JPL
247057.3 (0.1)	[20, 9, 12]→[19, 9, 11] A	-3.74	177.83	82	JPL
247057.7 (0.1)	[20, 9, 11]→[19, 9, 10] A	-3.74	177.83	82	JPL
247063.7 (0.1)	[20, 9, 12]→[19, 9, 11] E	-3.74	177.83	82	JPL
247124.3 (0.1)	[10, 5, 5]→[9, 4, 6] E	-4.74	49.08	42	JPL
258275.0 (0.1)	[21, 13, 8]→[20, 13, 7] E	-3.79	248.37	86	JPL
258277.4 (0.1)	[21, 13, 8]→[20, 13, 7] A	-3.79	248.37	86	JPL
258277.4 (0.1)	[21, 13, 9]→[20, 13, 8] A	-3.79	248.37	86	JPL
259341.9 (0.1)	[24, 0, 24]→[23, 1, 23] E	-4.37	158.23	98	JPL
259342.0 (0.1)	[24, 1, 24]→[23, 1, 23] E	-3.58	158.23	98	JPL
259342.1 (0.1)	[24, 0, 24]→[23, 0, 23] E	-3.58	158.23	98	JPL
259342.3 (0.1)	[24, 1, 24]→[23, 0, 23] E	-4.37	158.23	98	JPL
259342.7 (0.1)	[24, 0, 24]→[23, 1, 23] A	-4.37	158.22	98	JPL

Table 4 continued

Table 4 (*continued*)

Frequency (MHz)	Transition ^a	log(Einstein-A)	E_u (K)	g_u	Ref.
259342.9 (0.1)	[24, 1, 24]→[23, 1, 23] A	−3.58	158.22	98	JPL
259343.0 (0.1)	[24, 0, 24]→[23, 0, 23] A	−3.58	158.22	98	JPL
259343.2 (0.1)	[24, 1, 24]→[23, 0, 23] A	−4.37	158.22	98	JPL
261822.3 (0.1)	[17, 10, 7]→[17, 9, 8] A	−4.73	156.63	70	JPL
262088.2 (0.1)	[16, 10, 6]→[16, 9, 7] A	−4.76	146.59	66	JPL
262088.2 (0.1)	[16, 10, 7]→[16, 9, 8] A	−4.76	146.59	66	JPL
Methyl formate (CH ₃ OCHO $v = 1$)					
243511.5 (0.1)	[20, 12, 8]→[19, 12, 7] E	−3.85	407.25	82	JPL
245846.9 (0.1)	[21, 3, 19]→[20, 3, 18] E	−3.66	326.30	86	JPL
246106.8 (0.1)	[20, 7, 14]→[19, 7, 13] A	−3.70	343.77	82	JPL
246184.2 (0.1)	[20, 8, 13]→[19, 8, 12] E	−3.72	353.27	82	JPL
246187.0 (0.1)	[21, 2, 19]→[20, 2, 18] A	−3.66	326.62	86	JPL
246233.6 (0.1)	[20, 7, 13]→[19, 7, 12] A	−3.70	343.79	82	JPL
246274.9 (0.1)	[20, 7, 13]→[19, 7, 12] E	−3.70	343.86	82	JPL
246410.95 (0.01)	[10, 5, 5]→[9, 4, 6] A	−4.73	236.70	42	JPL
246422.7 (0.1)	[22, 1, 21]→[21, 2, 20] A	−4.51	330.43	90	JPL
246461.2 (0.1)	[22, 2, 21]→[21, 2, 20] A	−3.65	330.43	90	JPL
246488.4 (0.1)	[22, 1, 21]→[21, 1, 20] A	−3.65	330.43	90	JPL
246562.9 (0.1)	[21, 2, 19]→[20, 2, 18] E	−3.66	326.24	86	JPL
246706.5 (0.1)	[22, 2, 21]→[21, 2, 20] E	−3.65	329.89	90	JPL
246731.7 (0.1)	[22, 1, 21]→[21, 1, 20] E	−3.65	329.89	90	JPL
246985.2 (0.1)	[20, 6, 15]→[19, 6, 14] A	−3.68	335.37	82	JPL
259003.9 (0.1)	[21, 7, 14]→[20, 7, 13] A	−3.63	356.22	86	JPL
259025.8 (0.1)	[21, 7, 14]→[20, 7, 13] E	−3.63	356.29	86	JPL
260479.6 (0.1)	[44, 9, 36]→[44, 8, 37] A	−4.59	828.74	178	JPL
Dimethyl ether (CH ₃ OCH ₃)					
246499.29 (0.01)	[37, 6, 31]→[37, 5, 12] AA	−4.01	693.72	750	CDMS
246505.09 (0.01)	[37, 6, 31]→[37, 5, 12] AE	−4.01	693.72	450	CDMS
246505.09 (0.01)	[37, 6, 31]→[37, 5, 12] EA	−4.01	693.72	300	CDMS
246697.43 (0.01)	[27, 4, 23]→[26, 5, 21] AA	−4.70	367.61	330	CDMS
246697.87 (0.01)	[27, 4, 23]→[26, 5, 21] EE	−4.70	367.61	880	CDMS
246698.31 (0.01)	[27, 4, 23]→[26, 5, 21] AE	−4.70	367.61	110	CDMS
246698.31 (0.01)	[27, 4, 23]→[26, 5, 21] EA	−4.70	367.61	220	CDMS
259305.22 (0.01)	[33, 3, 31]→[34, 6, 28] AA	−6.61	563.02	670	CDMS
259308.39 (0.01)	[33, 3, 31]→[34, 6, 28] AE	−6.61	563.02	402	CDMS
259308.39 (0.01)	[33, 3, 31]→[34, 6, 28] EA	−6.61	563.02	268	CDMS
259309.47 (0.01)	[17, 5, 12]→[17, 4, 13] AE	−4.06	174.54	210	CDMS
259309.76 (0.01)	[17, 5, 12]→[17, 4, 13] EA	−4.06	174.54	140	CDMS
259311.95 (0.01)	[17, 5, 12]→[17, 4, 13] EE	−4.06	174.54	560	CDMS
259314.28 (0.01)	[17, 5, 12]→[17, 4, 13] AA	−4.06	174.54	350	CDMS
Acetone (CH ₃ COCH ₃)					
244218.91 (0.01)	[20, 5, 15]→[19, 6, 14] AE	−3.32	139.69	82	JPL
244218.91 (0.01)	[20, 6, 15]→[19, 5, 14] AE	−3.32	139.69	250	JPL
244218.92 (0.01)	[20, 5, 15]→[19, 6, 14] EA	−3.32	139.69	160	JPL
244218.92 (0.01)	[20, 6, 15]→[19, 5, 14] EA	−3.32	139.69	160	JPL
245831.34 (0.09)	[13, 10, 3]→[12, 9, 4] EE	−3.80	77.84	432	JPL
246400.99 (0.05)	[34, 7, 28]→[34, 5, 29] EE	−4.17	364.98	1100	JPL
246400.99 (0.05)	[34, 6, 28]→[34, 5, 29] EE	−4.03	364.98	1100	JPL
246400.99 (0.05)	[34, 7, 28]→[34, 6, 29] EE	−4.03	364.98	1100	JPL
246400.99 (0.05)	[34, 6, 28]→[34, 6, 29] EE	−4.17	364.98	1100	JPL
246404.27 (0.01)	[22, 3, 19]→[21, 4, 18] AE	−3.23	149.62	90	JPL
246404.27 (0.01)	[22, 4, 19]→[21, 3, 18] AE	−3.23	149.62	270	JPL
246404.29 (0.01)	[22, 3, 19]→[21, 4, 18] EA	−3.23	149.62	180	JPL
246404.29 (0.01)	[22, 4, 19]→[21, 3, 18] EA	−3.23	149.62	180	JPL

Table 4 *continued*

Table 4 (*continued*)

Frequency (MHz)	Transition ^a	log(Einstein-A)	E_u (K)	g_u	Ref.
246450.40 (0.01)	[22, 4, 19]→[21, 3, 18] EE	-3.23	149.57	720	JPL
246450.40 (0.01)	[22, 3, 19]→[21, 3, 18] EE	-5.09	149.57	720	JPL
246450.40 (0.01)	[22, 3, 19]→[21, 4, 18] EE	-3.24	149.57	720	JPL
246450.40 (0.01)	[22, 4, 19]→[21, 4, 18] EE	-4.92	149.57	720	JPL
246496.17 (0.46)	[25, 14, 12]→[24, 15, 9] AE	-5.01	257.11	100	JPL
246496.47 (0.02)	[22, 3, 19]→[21, 4, 18] AA	-3.23	149.51	270	JPL
246496.47 (0.02)	[22, 4, 19]→[21, 3, 18] AA	-3.23	149.51	450	JPL
246714.12 (0.05)	[9, 8, 1]→[8, 5, 4] EA	-5.84	40.59	76	JPL
246714.94 (0.05)	[32, 4, 28]→[32, 4, 29] EA	-3.97	305.61	260	JPL
246714.94 (0.05)	[32, 5, 28]→[32, 3, 29] EA	-3.97	305.61	260	JPL
246715.04 (0.05)	[32, 5, 28]→[32, 4, 29] AE	-3.97	305.61	390	JPL
246715.04 (0.05)	[32, 4, 28]→[32, 3, 29] EA	-3.97	305.61	130	JPL
246719.92 (0.04)	[33, 6, 28]→[33, 4, 29] EE	-5.62	344.85	1100	JPL
246719.92 (0.04)	[33, 5, 28]→[33, 4, 29] EE	-3.87	344.85	1100	JPL
246719.92 (0.04)	[33, 6, 28]→[33, 5, 29] EE	-3.87	344.85	1100	JPL
246719.92 (0.04)	[33, 5, 28]→[33, 5, 29] EE	-5.61	344.85	1100	JPL
261818.11 (0.01)	[20, 7, 13]→[19, 8, 12] EA	-3.31	151.17	160	JPL
261818.17 (0.01)	[20, 7, 13]→[19, 8, 12] AE	-3.31	151.17	82	JPL
261819.09 (0.01)	[20, 8, 13]→[19, 7, 12] EA	-3.31	151.17	160	JPL
261819.17 (0.01)	[20, 8, 13]→[19, 7, 12] AE	-3.31	151.17	250	JPL
Methyl cyanide (CH ₃ CN)					
257507.56 (0.01)	[<i>N</i> , <i>K</i>]=[14, 2]→[13, 2]	-3.00	121.28	58	JPL
257522.43 (0.01)	[<i>N</i> , <i>K</i>]=[14, 1]→[13, 1]	-2.99	99.84	58	JPL
257527.38 (0.01)	[<i>N</i> , <i>K</i>]=[14, 0]→[13, 0]	-2.99	92.70	58	JPL
Acetaldehyde (CH ₃ CHO $v_t = 0$)					
246330.73 (0.01)	[15, 3, 13]→[15, 2, 14] A	-4.29	131.49	62	JPL
260530.40 (0.01)	[14, 1, 14]→[13, 1, 13] E	-3.20	96.39	58	JPL
260544.02 (0.01)	[14, 1, 14]→[13, 1, 13] A	-3.20	96.32	58	JPL
260547.46 (2.07)	[9, 4, 5]→[9, 3, 7] E, $v_t = 2$	-6.06	456.38	38	JPL
gauche-Ethanol (<i>g</i> -C ₂ H ₅ OH)					
246414.76 (0.05)	[14, 3, 11]→[13, 3, 10] $v_t = 0 \rightarrow 0$	-3.89	155.72	29	JPL
246524.28 (0.01)	[13, 2, 12]→[12, 1, 12] $v_t = 0 \rightarrow 1$	-4.50	136.95	27	JPL
246658.18 (0.01)	[32, 5, 28]→[32, 4, 29] $v_t = 0 \rightarrow 0$	-6.33	527.94	65	JPL
246662.98 (0.01)	[4, 2, 3]→[3, 1, 3] $v_t = 1 \rightarrow 0$	-4.36	74.77	9	JPL
259322.64 (0.01)	[14, 3, 11]→[13, 2, 11] $v_t = 0 \rightarrow 1$	-4.39	155.72	29	JPL
260457.73 (0.01)	[15, 4, 12]→[14, 4, 11] $v_t = 1 \rightarrow 1$	-3.83	181.10	31	JPL
trans-Ethanol (C ₂ H ₅ OH)					
246663.62 (0.05)	[24, 1, 23]→[24, 0, 24]	-3.73	252.35	49	JPL
261815.99 (0.05)	[28, 3, 26]→[28, 2, 27]	-3.96	350.98	57	JPL
Glycolaldehyde (<i>cis</i> -CH ₂ OHCHO)					
246773.09 (0.02)	[30, 2, 28]→[30, 1, 29]	-4.04	252.68	61	CDMS
246778.28 (0.02)	[30, 3, 28]→[30, 2, 29]	-4.04	252.68	61	CDMS
262056.78 (0.01)	[25, 2, 24]→[24, 1, 23]	-3.34	158.25	51	CDMS
261795.48 (0.01)	[25, 11, 14]→[25, 10, 15]	-3.57	254.23	51	CDMS
261798.96 (0.01)	[25, 11, 15]→[25, 10, 16]	-3.57	254.23	51	CDMS
Methyl cyanide (CH ₂ DCN)					
259315.51 (0.01)	[15, 1, 15]→[14, 1, 14]	-2.82	104.97	31	CDMS
260523.05 (0.01)	[15, 2, 13]→[14, 2, 12]	-2.82	121.60	31	CDMS
Ethyl cyanide (CH ₃ CH ₂ CN)					
246268.74 (0.01)	[27, 2, 25]→[26, 2, 24]	-2.90	169.80	55	CDMS
246421.92 (0.01)	[28, 2, 27]→[27, 2, 26]	-2.90	177.26	57	CDMS
246548.70 (0.01)	[27, 3, 24]→[26, 3, 23]	-2.90	174.06	55	CDMS
260535.69 (0.05)	[29, 5, 25]→[28, 5, 24]	-2.84	215.06	59	CDMS
Formamide (NH ₂ CHO)					

Table 4 continued

Table 4 (*continued*)

Frequency (MHz)	Transition ^a	log(Einstein-A)	E_u (K)	g_u	Ref.
243521.04 (0.01)	[12, 1, 12]→[11, 1, 11]	−2.98	79.19	25	CDMS
Formic acid (<i>t</i> -HCOOH)					
262103.48 (0.01)	[12, 0, 12]→[11, 0, 11]	−3.69	82.77	25	CDMS

^aThe typical quantum numbers are listed as $[J, K_a, K_c]$ unless specified.

^bThe quantum numbers are $[N, J, F]$

C. THE SPECTRA OF CCH

The CCH spectra toward the continuum emission have irregular line profiles. Some spectra have strong self-absorption, while some spectra only show the blue-shifted emission. Due to the absorption and irregular line profile, the XCLASS fitting routine often fails to faithfully reproduce the observed CCH spectra. CCH can easily form in the outflow cavity wall due to the abundant CH_4 sublimated from dust grains as well as C^+ ionized by the UV radiation. Thus, the CCH spectra can have broad line width and multiple components. Furthermore, the morphology of the CCH emission traces the outflows, making our extraction from the continuum emission non-ideal for representing the nature of the CCH emission. Figure 13 and Y show the spectra and the moment 0 map of CCH, respectively.

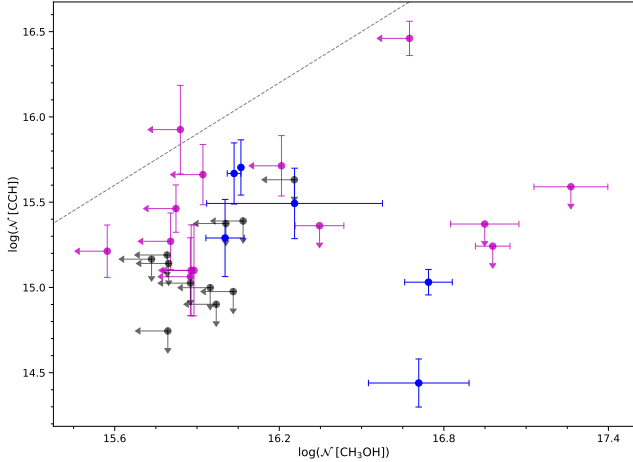


Figure 12. Correlation of the column densities of CCH and CH_3OH fitted from the PEACHES protostars. The sources where both molecules are detected are shown in black; the sources where only one molecule is detected are shown in magenta; finally, the sources where both molecules are not detected are shown in black for the corresponding upper limits.

D. NOTES ON THE COMS MODELING

E. NOTES ON THE 1D SPECTRA

Per-emb-33-A—

- The fitting of CH_3OCHO reproduces the the strongest emission at 259343 MHz, but underestimates the emission between 246275 MHz to 247070 MHz, where the emission is at most 0.5 K. Considering the narrow absorption in HCN, CS, and SO lines as well as the brighter continuum temperature (10.5 K), the emission of CH_3OCHO may be affected by the continuum opacity.

Per-emb-26—

- Red-shifted excess appears in the CH_3OH lines.
- Unidentified lines at 246525 MHz and 244249 MHz.

Per-emb-17—

- Many line profiles exhibit a broad double-peaked profile, separated by $\sim 5\text{--}6 \text{ km s}^{-1}$. *Per-emb-17* is a binary system unresolved by our observations. However, the channel maps suggest that the two components are likely to surrounding the southern source, *Per-emb-17-B*.
- The CH_3OCHO line at ~ 259343 MHz may be optically thick.

SVS13 A2—

- Weak indication of the unidentified line at 246525 MHz, which has been detected in other sources.

Per-emb-44—

- Unidentified lines at 244248 MHz, 246219 MHz, 246254 MHz, 246344 MHz, 246389 MHz, 246434 MHz, 246525 MHz, 246838 MHz, 258268 MHz, 258271 MHz, and 262068–262070 MHz.
- Higher temperatures ($T_{\text{ex}} > 100$ K) provide better fittings. Probably should adopt the temperature fitted from CH_3OCHO (previous MCMC fitting suggests a temperature of 263 K).

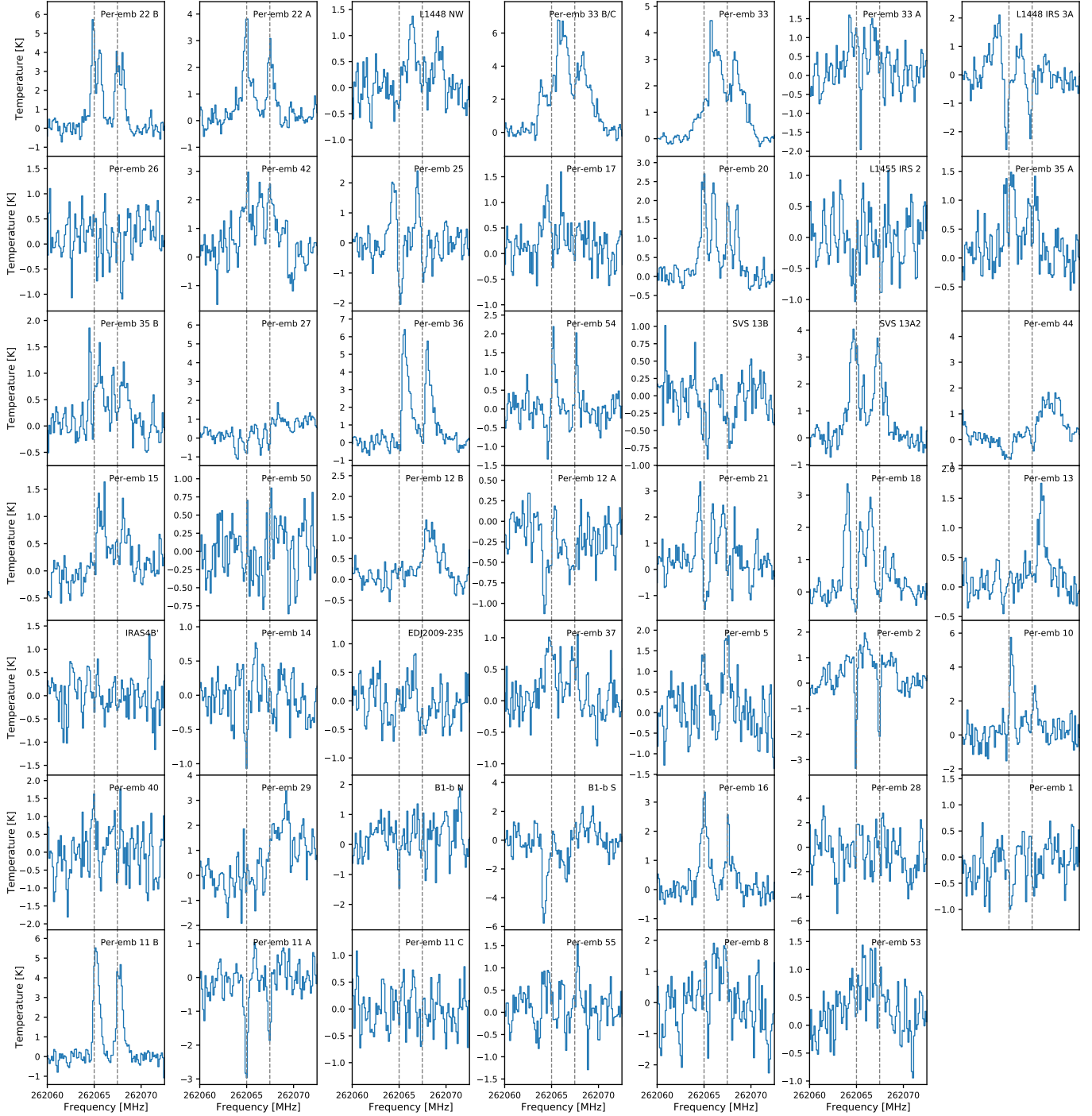


Figure 13. The CCH spectra of all PEACHES sources extracted from the continuum emission.

Per-emb-12-B—

- Unidentified lines at 244248 MHz, 246254 MHz, 246314 MHz, 246322 MHz, 246389 MHz, 246434 MHz, 246525 MHz, 246696 MHz, 246838 MHz, 246873 MHz, 247082 MHz, 258268 MHz, 258271 MHz, and 262068-262070 MHz.

Per-emb-12-A—

- Strong absorption features detected across the spectra, CCH, SO, H^{13}CN , CS, CH_3OH , HDCO, CH_3CN , and CH_3OCHO .

IRAS4B—

- Spectra show no emission along with absorption at SO, CS, and CH_3OH lines.

Per-emb-13—

- The CH_3OCHO emission needs $T_{\text{ex}} > 100$ K to have a good fit.
- All three CH_3OH lines are detected but two of them show clear sign of self-absorption, therefore, not ideal for fitting the excitation temperature.
- Unidentified lines at 244248 MHz, 246254 MHz, 246331 MHz, 246344 MHz, 246434 MHz, 246525 MHz, 246838 MHz, 246974 MHz, 247086 MHz, 257268 MHz, 257271 MHz, 259323 MHz, 259331 MHz, 262098 MHz, and 262109 MHz.
- The best-fitting model for $^{13}\text{CH}_3\text{OH}$ lines overestimates the line width due to the weak and broad line at 247086 MHz.

Per-emb-27—

- All three CH_3OH lines are detected, but none of the temperature produce a good fit to all three lines, suggesting that some lines are optically thick. The intensities of the transitions at 243916 MHz and 261806 MHz are ~ 30 K, while the intensity at 246873 MHz is about 24 K. They seems to be optically thick. In comparison, the continuum brightness temperature is only 5.8 K.
- Unidentified lines at 244232 MHz, 244248 MHz, 246207 MHz, 246254 MHz, 246388 MHz, 246435 MHz, 246525 MHz, 246538 MHz, 246838 MHz, 246973 MHz, 247084 MHz, and 259330 MHz.
- The CH_3OH line at 243916 MHz and the SO lines become optically thick at 100 K.

Per-emb-21—

- Emission of CH_3OH is detected. However, the broad width and noisy spectra lead to a bad fit. The best-fitting model has the maximum line width allowed, 3.5 km s^{-1} .

Per-emb-35-B—

- The CH_3OH line at 243915 MHz has an S/N of 1.2, but hints the existence of CH_3OH .

Per-emb-35-A—

- The goodness of fitting for the CH_3OH lines is a strong function of temperature, suggesting that the CH_3OH lines can indicate the T_{ex} .
- The CH_3OCHO line at 259342 MHz has an S/N of 1.8, but hint the existence of CH_3OCHO .

Per-emb-15—

- All lines have only the blue-shifted emission, making them blue-asymmetric.

Per-emb-18—

- Many transitions of CH_3OCHO are tentatively detected; however, none of them has $\text{S/N} > 3$. Currently categorized as non-detection.

B1-bS—

- Higher temperatures produce worse fittings to the CH_3OCHO lines. Previous MCMC fitting of the CH_3OCHO lines suggests a temperature of 58 K.
- The fitting of CH_3OCH_3 is limited by the minimum line width of 1.2 km s^{-1} .
- Unidentified lines at 246027 MHz, 246099 MHz, 246143 MHz, 246192 MHz, 246525 MHz, 246674 MHz, and 2467320 MHz.
- The CH_3OCHO lines around 258278 MHz and the H^{13}CN lines have a few dips within the line profile, suggesting absorption or just noisy spectra.

Per-emb-29—

- Only two CH_3OH lines are covered. Both lines have a strength of ~ 10 K, suggesting optically thick.

REFERENCES

- Aikawa, Y. 2013, Chemical Reviews, 113, 8961
- Belloche, A., Maury, A. J., Maret, S., et al. 2020, A&A, 635, A198
- Bottinelli, S., Ceccarelli, C., Lefloch, B., et al. 2004, ApJ, 615, 354
- Carney, M. T., Yıldız, U. A., Mottram, J. C., et al. 2016, A&A, 586, A44
- Endres, C. P., Schlemmer, S., Schilke, P., Stutzki, J., & Müller, H. S. P. 2016, Journal of Molecular Spectroscopy, 327, 95

- Graninger, D. M., Wilkins, O. H., & Öberg, K. I. 2016, *ApJ*, 833, 125
- Herbst, E., & van Dishoeck, E. F. 2009, *ARA&A*, 47, 427
- Higuchi, A. E., Sakai, N., Watanabe, Y., et al. 2018, *ApJS*, 236, 52
- Imai, M., Oya, Y., Sakai, N., et al. 2019, *ApJL*, 873, L21
- Imai, M., Sakai, N., Oya, Y., et al. 2016, *ApJL*, 830, L37
- Jørgensen, J. K., van der Wiel, M. H. D., Coutens, A., et al. 2016, *A&A*, 595, A117
- Lee, C.-F., Li, Z.-Y., Ho, P. T. P., et al. 2017, *ApJ*, 843, 27
- McGuire, B. A. 2018, *ApJS*, 239, 17
- Möller, T., Endres, C., & Schilke, P. 2017, *A&A*, 598, A7
- Müller, H. S. P., Schlöder, F., Stutzki, J., & Winnewisser, G. 2005, *Journal of Molecular Structure*, 742, 215
- Müller, H. S. P., Thorwirth, S., Roth, D. A., & Winnewisser, G. 2001, *A&A*, 370, L49
- Oya, Y., Sakai, N., López-Sepulcre, A., et al. 2016, *ApJ*, 824, 88
- Oya, Y., Sakai, N., Watanabe, Y., et al. 2017, *ApJ*, 837, 174
- Pickett, H. M., Poynter, R. L., Cohen, E. A., et al. 1998, *JQSRT*, 60, 883
- Sahu, D., Liu, S.-Y., Su, Y.-N., et al. 2019, *ApJ*, 872, 196
- Sakai, N., Sakai, T., Hirota, T., Burton, M., & Yamamoto, S. 2009, *ApJ*, 697, 769
- Sakai, N., Sakai, T., Hirota, T., & Yamamoto, S. 2010, *ApJ*, 722, 1633
- Sakai, N., Sakai, T., Hirota, T., et al. 2014, *Nature*, 507, 78
- Sakai, N., Oya, Y., López-Sepulcre, A., et al. 2016, *ApJL*, 820, L34
- Stephens, I. W., Dunham, M. M., Myers, P. C., et al. 2018, *ApJS*, 237, 22
- Stephens, I. W., Bourke, T. L., Dunham, M. M., et al. 2019, *ApJS*, 245, 21
- Tychoniec, L., Tobin, J. J., Karska, A., et al. 2018, *ApJS*, 238, 19
- Yang, Y.-L., Evans, Neal J., I., Smith, A., et al. 2020, *ApJ*, 891, 61